Magnetic Resonance Studies of Energy Storage Materials

by

Rafael Vázquez Reina

A dissertation submitted to the Graduate Faculty in Physics in partial fulfillment of the
requirements for the degree of Doctor of Philosophy, The City University of New York

2013

This manuscript has been read and accepted for the
Graduate Faculty in Physics in satisfaction of the
dissertation requirement for the degree of Doctor of Philosophy.

Prof. Steven G. Greenbaum

January 11, 2013
Date

Chair of Examining Committee

Prof. Steven G. Greenbaum

January 11, 2013
Date

Executive Officer

Prof. Ying-Chih Chen

Prof. Frank Owens

Prof. Sophia N. Suarez

Prof. Yuhang Ren

Supervisory Committee

THE CITY UNIVERSITY OF NEW YORK

Abstract

Magnetic Resonance Studies of Energy Storage Materials

by

Rafael Vázquez Reina

Adviser: Professor Steven G. Greenbaum

In today's society there is high demand to have access to energy for portable devices in different forms. Capacitors with high performance in small package to achieve high charge/discharge rates, and batteries with their ability to store electricity and make energy mobile are part of this demand.

The types of internal dielectric material strongly affect the characteristics of a capacitor, and its applications. In a battery, the choice of the electrolyte plays an important role in the Solid Electrolyte Interphase (SEI) formation, and the cathode material for high output voltage.

Electron Paramagnetic Resonance (EPR) and Nuclear Magnetic Resonance (NMR) spectroscopy are research techniques that exploit the magnetic properties of the electron and certain atomic nuclei to determine physical and chemical properties of the atoms or molecules in which they are contained. Both EPR and NMR spectroscopy technique can yield meaningful structural and dynamic information.

Three different projects are discussed in this dissertation. First, High energy density capacitors where EPR measurements described herein provide an insight into structural and chemical differences in the dielectric material of a capacitor. Next, as the second project, Electrolyte solutions where an oxygen-17 NMR study has been employed to assess the degree of preferential solvation of Li^+ ions in binary mixtures of EC (ethylene carbonate) and DMC (dimethyl carbonate) containing $LiPF_6$ (lithium hexafluo-

rophosphate) which may be ultimately related to the SEI formation mechanism. The third project was to study Bismuth fluoride as cathode material for rechargeable batteries. The objective was to study ^{19}F and ^{7}Li MAS NMR of some nanocomposite cathode materials as a conversion reaction occurring during lithiation and delithation of the BiF_3/C nanocomposite.

To my wife, family and friends for being there all the times…

Acknowledgements

I would like to thank Professor Steven G. Greenbaum for giving me the opportunity of pursuing my Ph.D. under his guidance. I also would like to thank Dr. Phillip Stallworth and Dr. Paul Sideris for giving me precious advice and help.

To my friends Sohan, Armando, Jaime, Kodi, Garbriel, Sufia, Victor, Marc, Laura and Tetinana thank you for making my graduate life joyful. My Spanish family who always showed me their love and support in every moment, Antonio y Lola, my uncles and cousins, and my guys who give me the real values of life, Carlos, Alfonso, Raul, Santi, Raul, Fernando, Juan Carlos, Pedro, Manu, Ricardo, Placido and the rest.

I am very grateful to my parents, Antonio y Lola, and my parents-in-law, Ram and Kalpana. They always let me know that they are proud of me, which motivates me to do my best. Their understanding and love encouraged me to work hard and continue pursuing a Ph.D. I owe my every achievement to all of them.

Last but not least, I am greatly indebted to my devoted wife Megha for being with me every moment sharing my happiness and sorrow. Her love and support without any complaint or regret has enabled me to complete this Ph.D thesis.

Contents

List of Tables

List of Figures

Chapter 1

Introduction

It has become increasingly important in today's society to have ready access to energy in different forms. With the rapid development phase of electronics, it is extremely important to develop new capacitors with high performance in small packages. Replacing batteries with capacitors in some devices to achieve high charge/discharge rates, i.e. the global trend of electronics miniaturization and military interests in different types of weapons and electronic transport applications [1], is a large venue for scientific research. The type of internal dielectric material, the structure of the plates and the device packaging all strongly affect the characteristics of the capacitor, and its applications.

Batteries are also becoming immensely important, by virtue of their ability to store electricity and make energy mobile for many household and industrial applications. New markets are being created for these batteries, notably for the purpose of powering portable electronics, and EV/HEV's. Lithium ion (Li-ion) battery fulfils many of these demands. Investigations of the properties and the arrangement of battery materials are necessarily important for performance improvements and many techniques have been employed for such kind of investigations.

Electron Paramagnetic Resonance (EPR) and Nuclear Magnetic Resonance (NMR) spectroscopy are research techniques that exploit the magnetic properties of the electron and certain atomic nuclei to determine physical and chemical properties of the atoms or molecules in which they are contained. Both EPR and NMR spectroscopy technique can yield meaningful structural and dynamic information.

EPR measures the absorption of microwave radiation from an unpaired electron when it is placed in a strong magnetic field, and it is an ideal technique to complement other analytical methods in a wide range of application areas as Physics, Chemistry, Materials Research, Biology and Medicine. EPR measurements described herein provide an insight into structural and chemical differences in the dielectric material of a capacitor.

NMR provides detailed information about the structure, dynamics, and chemical environment of molecules. The NMR spectrum is sensitive to a number of physical parameters that are related to a working cell/battery such as Li-ion mobility, electronic conductivity and changes of electronic structure of the cations involved in a redox process. Moreover, the integrated individual peaks of a NMR spectrum are proportional to the respective number of active nuclei and, therefore provides a quantitative analysis of the environment of the nucleus that is being probed.

Different projects related to energy storage technology in which EPR and NMR spectroscopy were utilized are discussed in this thesis:

1. High energy density capacitors.
2. Electrolyte solution.
3. Bismuth fluoride nanocomposite as a positive electrode material for rechargeable lithium batteries.

Chapter 2

High Energy Density Capacitors

2.1 Introduction

A *capacitor* (formerly known as *condenser*) is an electric circuit element used to store charge temporarily, consisting in general of a pair of conductors separated and insulated from each other by a dielectric. When there is a potential difference (voltage) across the conductors, a static electric field develops in the dielectric that stores energy and produces a mechanical force between the conductors.

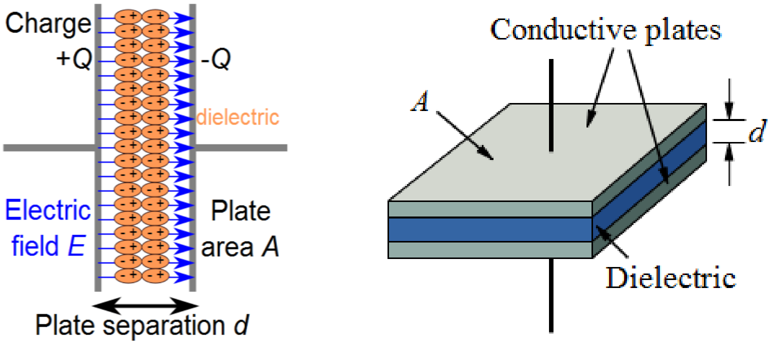

Figure 2.1.1: Parallel-Plate Capacitor

An ideal capacitor is characterized by a single constant value, capacitance. This is the ratio of the electric charge on each conductor to the potential difference between them. The capacitance is defined by the equation,

$$C = \frac{\epsilon A}{d} \tag{2.1.1}$$

where ε is the permittivity, A the area where the plates are extended assuming that the width of the plates is much greater than their separation d.

Capacitors capable of storing energy at high densities are being developed for use in filtering, noise reduction, pulse-power circuits in such diverse systems as defibrillators, particle-beam accelerators, microwave sources, and weapons. With the rapid development phase of electronics, it is extremely important to develop new capacitors with high performance in small packages.

2.2 Ceramic Capacitors

The capacitance is greatest in devices made from materials with a high permittivity, large plate area, and small distance between plates. However, the maximum energy storage using V_d as the dielectric (breakdown) strength, is given by

$$E = \frac{1}{2} \varepsilon A d V_d^2 \tag{2.2.1}$$

The storage energy is directly related to the dielectric material as the dielectric constant and the square of the dielectric strength V_d. In order to maximize the charge that a capacitor can hold, the dielectric material needs to have as high permittivity and breakdown voltage as possible.

Energy storage capacitors with reduced volume are increasingly in high demand for applications in mobile platforms including vehicles, airplanes and ships. The energy storage capability of a capacitor could be improved by increasing the energy density of the dielectric materials, as dielectrics occupy most of the volume of a capacitor.

Among various types of dielectric materials, of ceramics, plastic, polymers, composites, glass or mica, ceramics are the mostly widely used [1]. Plastics offer better stability and aging performance, which makes them useful in timer circuits, although they may be limited to low operating temperatures and frequencies. Glass and mica capacitors are extremely reliable, stable and tolerant to high temperatures and voltages, but are too expensive for most mainstream applications. Polymer dielectrics are inexpensive, light weight, and easy to produce commercially. In addition, polymers generally have high breakdown strengths, and are not prone to sudden catastrophic failure such as cracking from thermal or physical shock like ceramic capacitors. Unfortunately, polymers with high dielectric constants do not necessarily have high dielectric breakdown strengths.

Ceramic capacitors are generally small, cheap and useful for high frequency applications, although their capacitance varies strongly with voltage and they age poorly. The original ceramic capacitor design was disc-shaped, and with the exception of monolithic ceramic capacitors, that is still the predominant design. They are based on titanium dioxide but can also have levels of barium titanate or calcium titanate to increase the dielectric constant. They are not constructed in a wound configuration, like some other capacitors, so they can be used in high frequency applications.

Figure 2.2.1: Ceramic Capacitors

Ceramic capacitors are broadly categorized as Type I, Type II or Type III dielectrics:

- Type I ceramic capacitors are the most stable over voltage, temperature, and to some extent, frequency. They also have the lowest losses. Generally their dielectrics are made from a mixture of metal oxides and titanates, such as titanium dioxide but they can have low levels of barium titanate or calcium titanate. They have high insulation resistance and lower frequency losses and maintain a stable capacity even when voltage varies, and have predictable variation of capacitance with temperature. These are used in resonant circuits, filters and timing elements.

- Type II capacitors have less accuracy and stability. Their dielectrics are made from zirconates and titanates. They have somewhat higher losses of frequency and less insulation resistance than Type I capacitors, but can still maintain high capacity levels. They can operate at higher voltage. These are popular for use in coupling, blocking and filtering. One disadvantage of Type II capacitors is that they can lose capacity with age.
- Type III ceramic capacitors have poor accuracy and stability, and change in capacitance due to aging. These capacitors are adequate in applications which do not require high insulation resistance and capacity stability. They are made of ferroelectric materials such as barium titanate.

Due to the advantages of high dielectric constant ε, ceramic capacitors can easily achieve high capacitance density. However, high energy density cannot be readily accomplished without high dielectric breakdown strength and insulation resistance of the dielectrics [2].

Chapter 3

Electron Paramagnetic Resonance

3.1 Introduction

EPR, an acronym for **E**lectron **P**aramagnetic **R**esonance. EPR, also referred to as **E**lectron **S**pin **R**esonance (ESR) spectroscopy, measures the absorption of microwave radiation corresponding to the energy splitting of an unpaired electron having a net spin and angular momentum when it is placed in a strong magnetic field.

EPR was created after the development of the radar in World War II, and the first detection of an EPR signal was done by Zavoisky in 1945.

EPR is a spectroscopic technique that can yield meaningful structural and dynamic information, even from ongoing chemical or physical processes (i.e. kinetics, etc.) without influencing the process itself. This proves an ideal technique to complement other analytical methods in a wide range of application areas as Physics, Chemistry, Materials Research, Biology and Medicine.

3.2 How does EPR work?

The energy differences in EPR spectroscopy are predominately due to the interaction of unpaired electrons in the sample with a magnetic field produced by a magnet in the laboratory. This effect is called the *Zeeman Effect*.

Every electron has a magnetic moment and spin quantum number s = 1/2, with magnetic components (or precessing spin orientations) $m_s = +1/2$ and $m_s = -1/2$. In the presence of an external magnetic field with strength B_0, the electron's magnetic moment aligns itself either parallel ($m_s = -1/2$) or antiparallel ($m_s = +1/2$) to the field, each alignment having a specific energy. This effect creates two distinct energy levels for the unpaired electrons, and it should be possible to induce transitions between these electronic spin energy levels by subjecting the electrons to electromagnetic radiation equal in frequency to their precessional frequency.

The separation between the lower and upper energy states can be defined by the equation:

$$\Delta E = g_e \mu_B B_0 \tag{3.2.1}$$

where g_e is the electron's so-called g-factor and μ_B is the Bohr magneton, with the splitting of the energy levels being directly proportional to the magnetic field strength.

An unpaired electron can move between the two energy levels by either absorbing or emitting electromagnetic radiation of energy $\varepsilon = h\nu$ such that the resonance condition, $\varepsilon = \Delta E$, is obeyed. From Quantum Mechanics we obtain the most basic equations of EPR:

$$E = g\,\mu_B\,B_0\,m_s = \pm \tfrac{1}{2}\,g\,\mu_B\,B_0 \qquad \Delta E = h\nu = g\,\mu_B\,B_0 \tag{3.2.2}$$

where g is the g-factor, μ_B the Bohr magneton, and m_s the magnetic spin quantum number. When this equation applies, we say that the resonance condition applies.

By increasing an external magnetic field, the gap between the $m_s = +1/2$ and $m_s = -1/2$ energy states is widened until it matches the energy of the microwaves. At this point the unpaired electrons can transition between their two spin states. Since there are more electrons in the lower state, due to the Boltzmann distribution, there is a net absorption of energy, and it is this absorption which is monitored and converted into a spectrum.

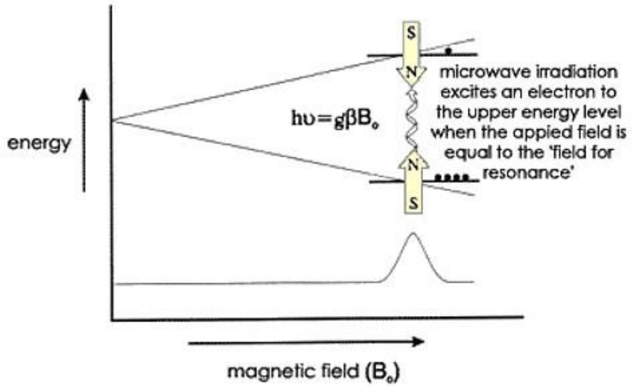

Figure 3.2.1: EPR absorption

To obtain the spectra one usually keeps the electromagnetic radiation frequency constant and scans the magnetic field. A peak in the absorption will occur when the magnetic field "tunes" the two spin states so that their energy difference matches the energy of the radiation.

The intensity of an EPR signal depends on the ability of the spin system to absorb photons of electromagnetic radiation. It is also important if we want to measure the concentration of the EPR active species in our sample. In the language of spectroscopy, the size of a signal is defined as the integrated intensity, i.e., the area beneath the absorption curve, which is proportional to the concentration.

EPR spectra are normally presented as plots of the first derivative of the energy absorbed from an oscillating magnetic field at a fixed microwave frequency versus the magnetic field strength to improve the signal-to-noise ratio. Magnetic field modulation (often at 100 KHz) is used in EPR to encode the EPR signal at the modulation frequency so that subsequent phase-sensitive detection discards most of the noise except that in a narrow band near the modulation frequency. EPR spectrometers use a phase-sensitive detector such that the first-harmonic output is the first derivative of the magnetic resonance absorption.

3.3 g Factor

The g factor is designated as the signal position parameter in EPR spectroscopy (as the chemical shift for NMR). Its knowledge can give information about a paramagnetic center's electronic structure.

An unpaired electron responds not only to a spectrometer's applied magnetic field B_0, but also to any local magnetic fields of atoms or molecules. The effective field B_{eff} experienced by an electron is thus written

$$B_{\mathrm{eff}} = B_0\,(1 - \sigma) \qquad (3.3.1)$$

where σ includes the effects of local fields (σ can be positive or negative).

The resonance condition is applied by $h\nu = g_e\mu_B B_{\mathrm{eff}} = g_e\mu_B B_0(1 - \sigma)$ when the energy of the microwave radiation match or is equal to the difference of energy states for the electron. The value of g for a free electron (g_e) is a well-known constant, 2.0023 [1]. The quantity $g_e(1 - \sigma)$ is denoted g and called simply the g-factor. So, the final resonance equation becomes,

$$h\nu = g\mu_B B_0 \quad \text{or} \quad g = \frac{h\nu}{\mu_B B_0} \qquad (3.3.2)$$

If g does not equal g_e the implication is that the ratio of the unpaired electron's spin magnetic moment to its angular momentum differs from the free electron value. Since an electron's spin magnetic moment is constant (approximately the Bohr magneton, $\mu_S = -g_S\mu_B(S/\hbar)$), then the electron must have gained or lost angular momentum through spin-orbit coupling. The magnitude of the change gives information about the nature of the atomic or molecular orbital containing the unpaired electron.

3.4 Hyperfine Coupling

Another important interaction in EPR is the Hyperfine Coupling. The unpaired electron, which gives us the EPR spectrum, is very sensitive to their local surroundings. The nuclei of the atoms in a molecule or complex often have a magnetic moment, which produces a local magnetic field at the electron. The resulting interaction between the electron and the nuclei is called *hyperfine interaction*.

The interaction expands the equation for the energy states (Eq. 3.2.2) of the electron and spin Hamiltonian with a new term, which represents the coupling between the nuclear and electronic spin magnetic moments:

$$E = g\, \mu_B\, B_0\, m_s + \mathbf{a}\, m_s\, m_I \tag{3.4.1}$$

$$\hat{H} = g\, \mu_B\, B_0\, \hat{S} + \hat{S}\, \tilde{\hat{\mathbf{A}}}\, \hat{I} \tag{3.4.2}$$

where **a** is the hyperfine coupling constant, m_s the electronic spin quantum number, m_I the nuclear spin quantum number for the neighboring nucleus, S the electron spin and I the nuclear spin.

Hyperfine Coupling is represented by separation between the lines of a multiplet in an EPR spectrum, and its symbol **a** is expressed in the dimension of energy. The sign and magnitude of a given value **a** depends on the proximity of the unpaired electron to the coupling nuclei.

A single nucleus with a spin ½, for example, will split each energy level into two, as shown below, and then two transitions (or absorptions) can be observed.

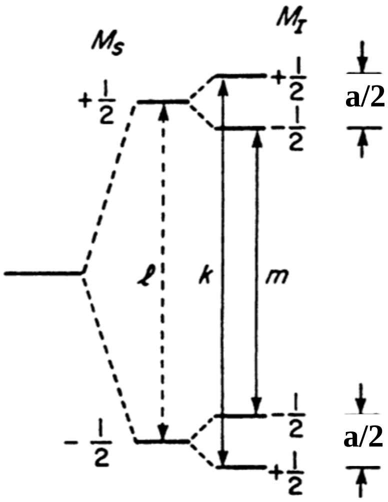

Figure 3.4.1: Energy Levels

The energy difference between the two absorptions is equal to the hyperfine coupling constant **a** related to the spectral line spacing:

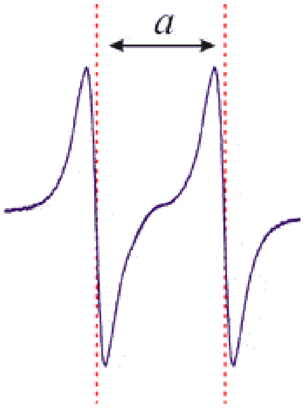

Figure 3.4.2: Hyperfine coupling constant

The number of lines which result from the coupling can be determined by the quantity 2I + 1, where I is the nuclear spin.

Hyperfine Coupling gives us wealth information about our sample such as the identity and number of atoms which make up a molecule or complex as well as their distances and orbital overlap from the unpaired electron. The g-factor and hyperfine coupling in an atom or molecule may not be the same for all orientations of an unpaired electron in an external magnetic field. This anisotropy depends upon the electronic structure of the atom or molecule in question, and so can provide information about the atomic or molecular orbital containing the unpaired electron. For systems with more than one unpaired electron (S>1/2) the ground state can be split in the absence of an external magnetic field due to the local site symmetry, the *zero-field splitting*. However, this does not apply to the systems studied here and therefore, will not be discussed further.

Chapter 4

EPR Study of TiO_2 Ceramics

4.1 Introduction

Previous research showed that titanium dioxide (TiO_2) ceramics as a dielectric material with nanosized structure possessed much higher Dielectric Breakdown Strength (*DBS)* and higher dielectric constant than conventional microsized TiO_2, making them suitable for energy storage applications in high energy density capacitors [1]. It was also found that the dielectric properties of TiO_2 are greatly affected by impurities (dopants) and defects [2] as well as processing conditions [3].

Titanium dioxide (TiO_2) is found in three crystalline phases: anatase, rutile and brookite, as well as in an amorphous phase. The rutile phase is the most common and stable form [4, 5]. Anatase and brookite both convert to rutile upon heating [6]. TiO_2 can be synthesized as single crystals, polycrystalline powders, ceramics and polycrystalline thin films. Transition metal oxides are often nonstoichiometric and at near-atmospheric oxygen pressure the oxygen vacancy is the predominant defect in TiO_2. The oxygen deficiency introduces an excess of electrons in the material resulting in an increase of the electrical conductivity [7].

Defects on the TiO_2 (110) surface are easily created by electron bombardment, sputtering, or simply by thermal annealing to high temperatures. Thermally created defects have been recognized extensively in the literature as point defects that exist as oxygen vacancy sites located within the bridging oxygen rows of the TiO_2(110) surface [8]. Macroscopically, the presence of oxygen vacancies creates an overall reduced state of the TiO_2 crystal, both in the bulk and in the surface. Upon annealing, the creation of defects within the bulk is associated with the creation of color centers and Ti^{+3} interstitial ions, and an overall reduced stoichiometry as a result of the loss of oxygen atoms. This effect occurs on the surface as well, where the presence of an oxygen vacancy site leaves an exposed Ti^{+3} ion which may be visualized as a Ti^{+4} ion associated with a somewhat localized electron [9]. The nonstoichiometry of the main structural phase of TiO_2 (rutile) and its natural n-type conductivity is due to oxygen deficiency, which has been explained in terms of native defects, i.e. oxygen vacancies and titanium interstitials (attributed to a shallow donor) [10-12]. TiO_2 is generally considered to be an insulator at temperatures less than 200 ˚C.

The majority of dopants enhance the *n*-type semiconducting properties of TiO_2. These dopants include niobium (Nb), tantalum (Ta), vanadium (V), fluorine (F), and hydrogen (H). Dopants that change the film to being *p*-type include aluminium (Al), iron (Fe), and indium (In) [5]. There are several motivations for introducing dopant atoms into thin films of TiO_2, which include altering the electrical conductivity, photoelectric response, chemical resistance, optical properties, melting temperature, and the resulting TiO_2 crystalline phase, as well as using the film as a dopant source. In this work, the primary motivation is to enhance the dielectric breakdown strength, DBS.

Titanium Dioxide has a lot of applications. In powders, it can be found as a white pigment in paint (called titanium white), plastic, inks, paper, and cosmetics; in washing powder, toothpaste, sunscreen, foodstuffs, pharmaceuticals, photographic plates, for creating synthetic gemstones; and as a catalyst. It is also used in thin films, for ultra-thin capacitors and MOSFETs due to its extremely high dielectric constant; as humidity and oxygen sensor due to the dependence of its electrical conductance on the gases present; as an optical coating and a material for waveguides due to its high refractive index; as a protective coating and corrosion resistant barrier; and as a photoanode in solar cells due its photoelectric activity.

The dielectric properties of TiO_2 are affected by defects and impurities (whether “native” or dopants) [2] as well as processing conditions [3]. In order to further clarify the effect of the dopants on the microstructure development and resultant dielectric properties of TiO_2, electron paramagnetic resonance (EPR) spectroscopy was employed in this study. This study was part of a collaboration with Dr. Sheng Chao, Dr. Vladimir Petrovsky and Prof. Fatih Dogan from Missouri University of Science and Technology, who provided the samples and made Impedance Spectroscopy measurements on them.

4.2 Experimental

For this project we are interested in Titanium Dioxide as a dielectric material for an energy storage capacitor. EPR measurements were performed at 77°K on powdered samples on a Bruker EMX spectrometer and, all the samples have been run under identical spectrometer settings. First-derivative spectra were obtained with 100 kHz field modulation and 3.00 Gauss modulation amplitude. Quartz EPR tubes of 4 mm diameter were filled with about 0.75 cm of material height. The quartz tube was placed inside of a crystal dewar filled with liquid nitrogen. All the EPR intensity data were normalized by weight and the measurements were taken at 9.40 GHz.

Two different types of TiO_2 powders with various types and amount of impurities were used in this study. Powder A (Nano) and powder B (TOHO) were obtained from Nanophase Technologies Corporation (Romeoville, IL) and Toho Titanium Co. Ltd. (Chigasaki, Japan), respectively.

Several Titanium Dioxide samples were investigated, including undoped and annealed in different environment as O_2 and N_2, doped with Vanadium (V), and doped with Manganese (Mn). The samples were crushed into powder to perform EPR Spectroscopy.

EPR signals arise from paramagnetic impurities, whether residual or intentional (from doping) or from paramagnetic defects such as dangling bonds. The oxygen vacancy is the predominant defect in TiO_2 and has an associated EPR response [13]. The oxygen deficiency introduces an excess of electrons in the material resulting in an increase of the electrical conductivity and dielectric loss [14], which has a deleterious effect on the material's breakdown strength and insulation resistance. Besides high breakdown strength, such capacitors require high insulation resistance for efficient charge storage under applied electrical field. In order to better understand the electrical effects of incorporated dopants such as Mn^{2+}, EPR was run to determine whether the dopants are well dispersed in the bulk or segregated at the grain boundaries, which will have a significant effect on electrical properties. Since the leakage current is closely related to dielectric breakdown phenomenon and the dielectric loss (particularly at low frequencies), reduction of electrical conductivity is of critical importance for successful application of dielectric materials in high energy density capacitors.

4.3 Results and Discussion

EPR spectra of undoped Nano TiO_2 are depicted in Figure 4.3.1. Nano undoped in O_2 shows a big peak around 3400 Gauss ($g \approx 2.043$) which is attributed to the oxygen vacancy in TiO_2 [9].

A hyperfine splitting is clearly recognizable. This hyperfine coupling may be attributed to Fe^{+3} substituted for Ti^{+4} in the TiO_2 (rutile) lattice, therefore the difference in charge in the crystal has to be compensated by the introduction of defects such as oxygen vacancies and different types of interstitial ions [15]. Iron is present as an impurity in the as-received material. Fe^{+3} ions may be incorporated into the crystal lattice of TiO_2 [12, 16]. Some peaks may be due to hyperfine coupling of Ti [13]. There are two isotopes of Ti with nuclear spin, i.e. Ti^{47} and Ti^{49} with $I = 5/2$ and $I = 7/2$ respectively, and isotopic abundances of 7.44% and 5.41% splitting from Ti^{47} and Ti^{49}.

Around 3200 Gauss ($g \approx 2.099$) we distinguish three clear peaks, and another pattern around 2000 ($g \approx 3.469$) and 2600 Gauss ($g \approx 2.668$), which are related to Fe^{+3} ion impurities [12,17,18]. The peaks between 450 Gauss ($g \approx 15.420$) and 1450 Gauss ($g \approx 4.785$) follow the same pattern for all Nano materials, and may be produced by other impurities.

Nano undoped and annealed in N_2 presents an interesting EPR signal. It has a broad and intense EPR signal around 3450 Gauss ($g \approx 1.947$) as the Nano undoped in O_2 but with no hyperfine structure, which suggests that there are high concentrations of oxygen vacancies which produce a large signal broadened by spin-spin interaction between neighboring paramagnetic centers. The absence of O_2 in the annealing atmosphere is likely to be accompanied by enhanced oxygen vacancy formation [19]. Also, the gain settings were much different in the two spectra with no presence of impurities in the case of Nano material undoped and annealed in N_2.

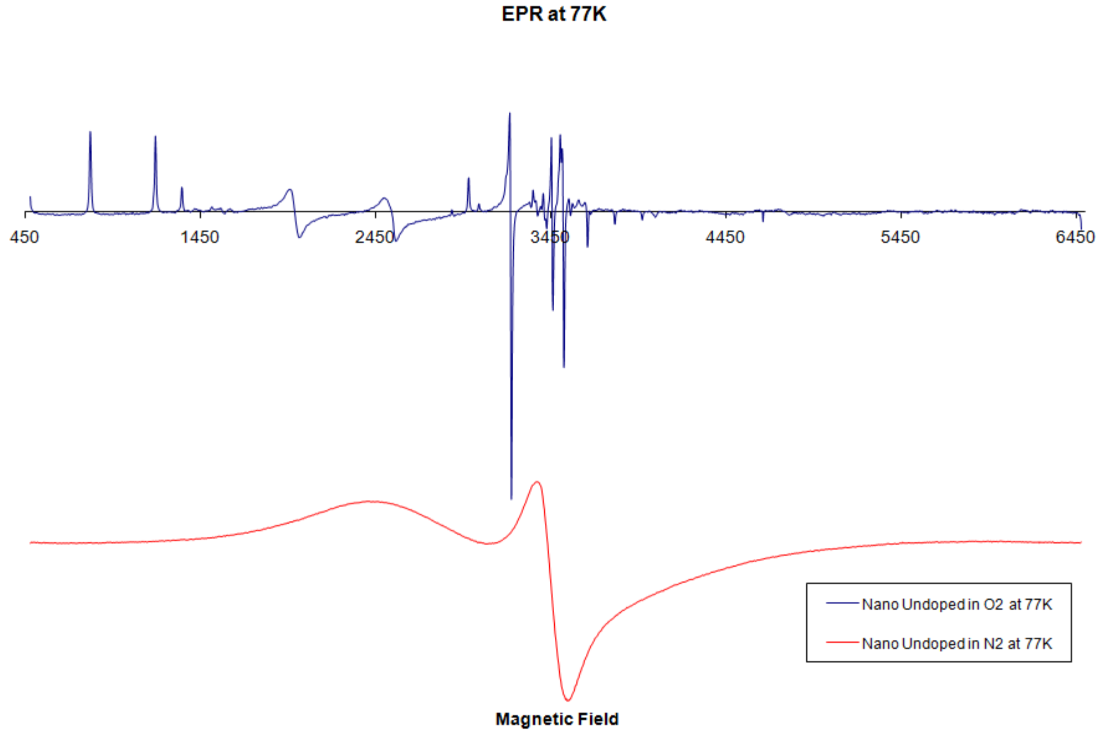

Figure 4.3.1: Nano undoped in O_2 and Nano undoped in N_2 at 77°K

EPR spectra of Vanadium-doped TiO_2 are depicted in Figure 4.3.2. Nano doped with Vanadium shows the typical hyperfine structure of 8 lines produced by the spin 7/2 of Vanadium [20, 21]. The hyperfine coupling of ^{51}V nuclei may indicate that the dopant ions are dispersed in the crystal host. This finding of interest to dielectric applications because it can distinguish between bulk doping and segregation of dopants at grain boundaries. Also the lightly doped (0.05%) sample presents a simple superposition of the signal from the native defects, impurities and the Vanadium dopant.

For Nano doped with higher Vanadium concentration (2%) we still see the Vanadium hyperfine splitting but in a severely broadened signal. This broadening is attributed to spin-spin interactions due to the high vanadia concentration. Also, Nano material doped with vanadium at 2% had different gain setting than the vanadium-doped at 0.05%, with no presence of impurities.

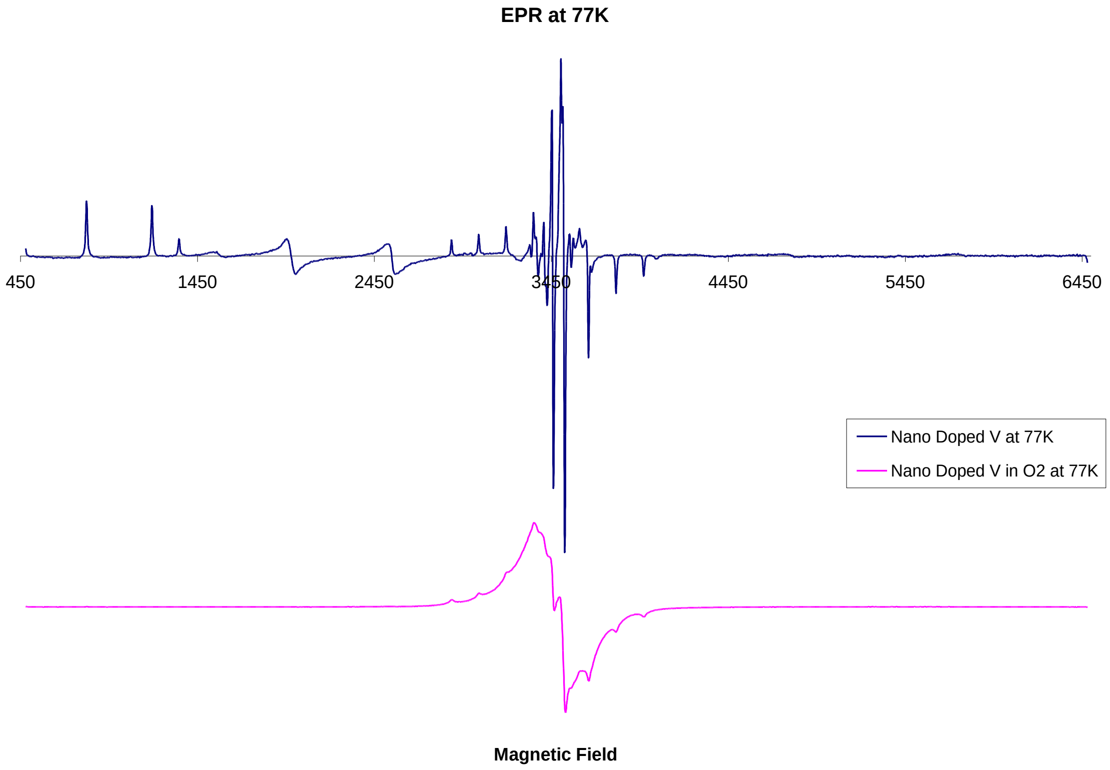

Figure 4.3.2: Nano doped with Vanadium (0.05%) and Nano doped with Vanadium (2%) at 77°K

EPR spectra of undoped and Mn-doped Toho TiO_2 are depicted in Figure 4.3.3. The undoped sample gives a spectrum indistinguishable from cavity background. There are no features commonly observed due to the presence of Fe impurities nor is there a signal attributable to oxygen vacancies, indicating that the density of these impurities and defects is significantly less than 10^{15} cm^{-3}.

Disc-shaped samples were sintered in oxygen atmosphere at 900ºC and 1100ºC for 2 hours. Mn-doped sample annealed at 900ºC presents only a relatively weak and broad resonance around 3000 Gauss. However, if the Mn^{+4} or Mn^{2+} ions were well dispersed in the structure one would expect a typical six-line pattern due to the hyperfine interaction associated with the spin-5/2 ^{55}Mn nucleus [17]. This result could be interpreted as the manganese ions not being uniformly incorporated into the TiO_2 structure, but rather clustered along the grain boundaries and therefore consistent with the impedance results.

In order to test this assertion, an EPR spectrum was also obtained for the same Mn-doped sample subjected to a post-anneal at 1100ºC. In this case there are a rich spectral features centered around 1250 Gauss and 3300 Gauss. Care was taken not to exposed the sample to additional possible paramagnetic impurities during the post-anneal so it is believed that the principal effect of the higher temperature is to facilitate diffusion of the dopant ions throughout the bulk of the sample. The spectrum shows multiple sites with clear hyperfine structure. The higher temperature annealing alters the distribution of the dopant ions to one that is more uniform throughout the bulk, which verifies our initial hypothesis that the 900ºC annealed sample has a non-uniform distribution of Mn ions. In the 1100ºC sample, there are two groups of g-values with 6 lines each overlapping. An essentially identical spectrum has been reported in Mn-doped TiO_2 and assigned to subtitutionally incorporated Mn^{+4}, in which the fine structure term splits the multiples into a double sextet resonance at 1000-1500 Gauss ($g \approx 4$) and another at around 3000 Gauss ($g \approx 2$) [22].

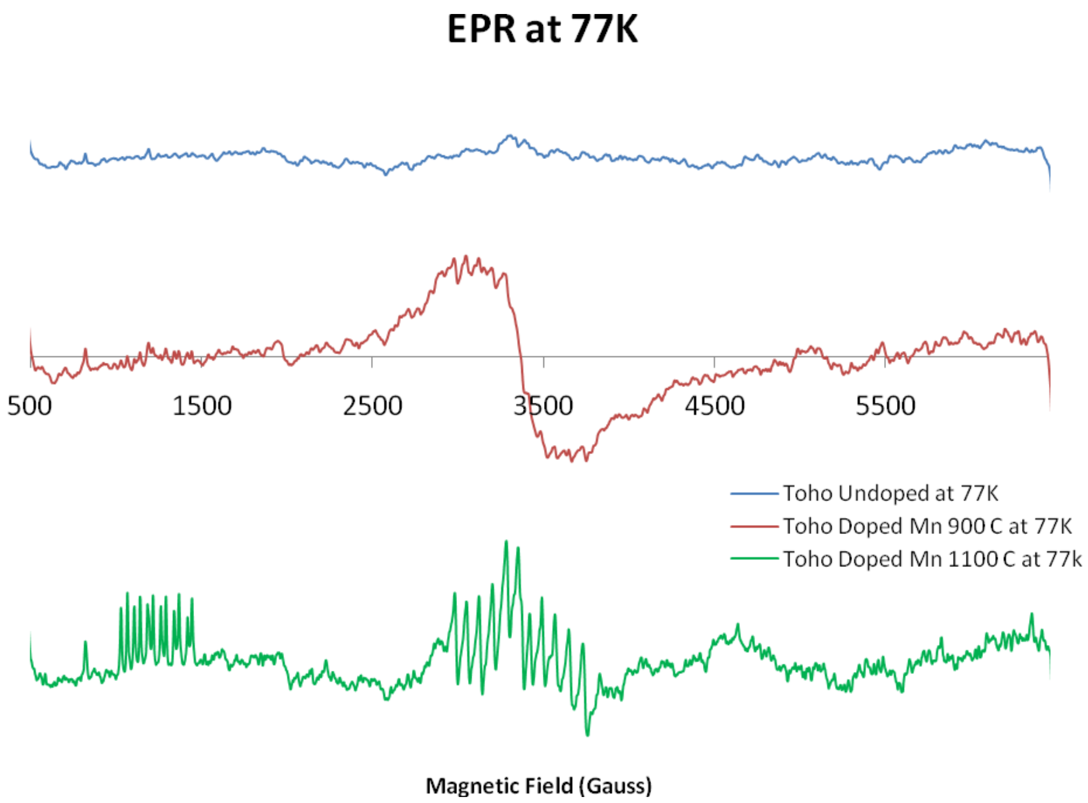

Figure 4.3.3: Toho undoped and Toho doped with Manganese at 77°K

A simulation was done by WinEPR-SimFonia software to confirm the hyperfine splitting of the two groups of g-values with 6 lines each overlapping and, assigned to subtitutionally incorporated Mn^{+4} as the reference stated. The hyperfine coupling constant **a** value was 5 Gauss for the simulation depicted in Fig. 4.3.4.

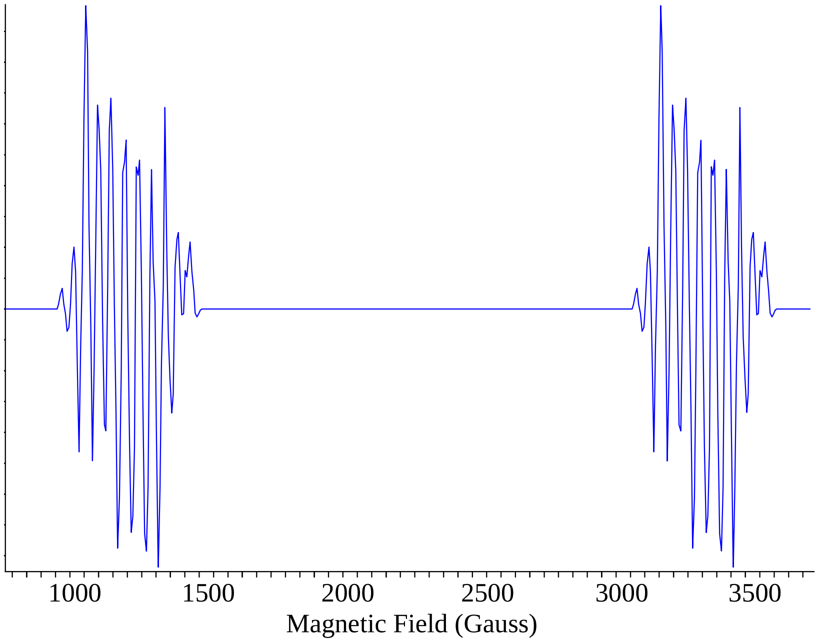

Figure 4.3.4: Simulation

Despite the complexity of this spectrum, the main purpose here is to demonstrate that the lower temperature annealing process leaves the dopant ions segregated at the grain boundaries or otherwise clustered.

Because TiO_2 powder was doped by surface coating of the particles, clustering of Mn-ions at the grain boundaries occurs at low sintering temperatures. With the increase of sintering temperature, Mn-ions diffuse from the grain boundaries into the TiO_2 grains. The binding nature and preferential sites between Mn-ions and TiO_2 is governed by the interfacial reactions according to the phase equilibria in the MnO-TiO_2 system. The diffusion process during the initial stage of interfacial reactions may lead to formation of localized phases such as $MnTiO_3$, Mn_2TiO_4 or $MnTi_2O_5$ along the grain boundary region. Further increase of sintering temperature and time would result in diffusion of Mn-ions into the TiO_2 grains and dilution of dopant concentration within the grain boundaries. Further studies by utilizing of electron microscopy techniques are needed to reveal the nature and distribution of Mn- and Ti-ions along and near the grain boundaries of nanostructured TiO_2 dielectrics toward better understanding of the relationship between their electrical properties, microstructural evolution and defect structure.

The effect of Mn doping on the dielectric properties of TiO_2 was reported in [23]. An optimized concentration of about 0.05 mol% led to reduced conductivity and loss tangent as well as improved voltage breakdown strength and energy storage capability of the dielectric due to generation of possible electron traps. Further increase of Mn content resulted in higher dielectric loss due to formation of oxygen vacancies. Increased grain-boundaries resistivity was observed with higher Mn-doping concentration, presumably due to segregation of Mn solutes at the grain boundaries. Larger difference between the grain-boundary conductivity gave rise to space charge polarization.

A decrease in conductivity by appropriate amount of Mn doping is attributed to creation of electron traps due to the fact that Mn^{+4} and Mn^{+3} have higher tendency for reduction as compared to Ti^{+4} in dielectric ceramics such as $BaTiO_3$ [24]. However, excessive doping of TiO_2 with Mn ions would result in a decrease of resistivity by formation of oxygen vacancies.

EPR studies confirmed that improvement of insulation resistance is correlated with a non-uniform distribution of dopant ions, concentrated at the grain boundaries. The insulation resistance of the sample sintered at 900ºC was higher than that of the sample sintered at 1100ºC.

4.4 Conclusion

Nanostructured TiO_2 has shown promise as a dielectric material for high energy density ceramic capacitors because of its high dielectric breakdown strength and dielectric constant. Strategies to increase the insulation resistance or to reduce the leakage current of TiO_2 include doping with transition metal ions.

EPR measurements provided an insight into structural and chemical differences in these materials. TiO_2 samples give a hyperfine coupling for certain dopants, and show the interaction of some impurities that may play an important role in TiO_2 as dielectric material.

Commercial Nano (manufacturing designation) materials show lots of impurities and great concentration of oxygen vacancies, which are not appreciable in the Toho samples. Nano undoped material shows the highest peak around 3400 Gauss ($g \approx 2.043$), which is attributed to oxygen vacancy. Vanadium-doped and Mn-doped TiO_2 showed the hyperfine splitting characteristics of the ^{51}V and ^{55}Mn nuclei respectively, indicating that the dopant ions were dispersed in the host crystal. However, Mn-doped annealed at 900°C shows that the Mn centers are clustered, and when annealed at 1100°C are dispersed as for the vanadium case. Manganese dopant hyperfine structure shows two groups each of two g-values overlapping given eleven lines of hyperfine structure assigned to subtitutionally incorporated Mn^{+4}.

This study is combined with other techniques, such as impedance spectroscopy and scanning electron microscopy of Mn-doped nanoscopic TiO_2, demonstrate that sintering at 900 °C leads to optimal electrical properties that are correlated with a non-uniform distribution of dopant ions, concentrated at the grain boundaries. Nanostructured TiO_2 dielectrics with improved insulation resistance are promising for the development of higher energy density capacitors.

Chapter 5

Batteries

5.1 Introduction

It has become increasingly important in today’s society to have ready access to energy in different forms. Batteries are therefore becoming immensely important, by virtue of their ability to store electricity and make energy mobile.

A battery is one or more electrochemical cells that convert chemical energy directly into electrical energy. Since the invention of the first battery (or "voltaic pile") in 1800 by Alessandro Volta, batteries have become a common power source for many household and industrial applications. A number of cells are connected in series or parallel or both depending on the voltage and capacity requirement. A cell is just the working chemical unit inside a battery and, it has three main parts: a positive electrode (cathode), a negative electrode (anode), and a liquid or solid separating them called the electrolyte.

In the redox reaction that powers the battery, cations are reduced (electrons are added) at the cathode, while anions are oxidized (electrons are removed) at the anode. The electrodes do not touch each other but are electrically connected by the electrolyte, which allows ions to flow.

Figure 5.1.1: Types of Batteries

There are two types of batteries: primary batteries (disposable batteries), which are designed to be used once and discarded, and secondary batteries (rechargeable batteries), which are designed to be recharged and used multiple times.

Primary batteries are most commonly used in portable devices that have low current drain, used intermittently and used well away from an alternative power source, such as in alarm and communication circuits where other electric power is only intermittently available. Since the chemical reactions are not easily reversible and active materials may not return to their original forms, disposable primary cells cannot be reliably recharged. Zinc-carbon batteries and alkaline batteries are common types in this category.

Secondary batteries must be charged before use and they are usually assembled with active materials in the discharged state. Rechargeable batteries or secondary cells can be recharged by applying electric current, which reverses the chemical reactions that occur during its use. There are a vast number of battery types in the rechargeable category such as lead-acid and Li-ion battery types.

5.2 Cell

A cell consists of three major components:

1. The anode or the negative electrode, which gives up electrons to the external circuit and is oxidized during the electrochemical reaction.

2. The cathode or the positive electrode, which accepts electrons from the external circuit.

3. The electrolyte, which acts as an ionic conducting medium which provides the transfer of charge (ions) inside the cell between anode and cathode. Typically, for a lithium ion cell, a liquid electrolyte is a solution of a solvent such as ethylene carbonate (EC) and ethylmethyl carbonate (EMC) with dissolved salt ($LiPF_6$, $LiAsF_6$, etc...) in it.

If a load is connected externally to the electrodes of a cell, electrons will flow under the influence of a difference in potential across the electrodes from the anode through the external conductor to the cathode.

The voltage across the electrodes depends primarily upon the materials from which the electrodes are made and to a lesser extent the composition of the electrolyte. The current that a cell delivers depends upon the resistance in the entire circuit, including the cell itself. The internal resistance of the cell depends upon the size the electrodes, the distance between them in the electrolyte, and the resistance of the electrolyte.

The theoretical voltage/potential of a cell is determined by the type of the active material used in the cell and calculated from free-energy data. The decrease in the Gibbs free-energy of a chemical reaction is given by,

$$\Delta G^0 = - n\, F\, E^0 \tag{5.2.1}$$

where *F* is the Faraday constant (~ 96,500 C or 26.8 Ah), *n* is the number of electrons per mole of product and E^0 is the standard electrode potential of the reaction. Standard electrode potentials of some active materials are listed in Table 5.1.

Material	Atomic or molecular mass, g	Standard reduction potential at 25 ^{0}C, V	Valence change
Li	6.94	-3.01	1
Na	23.0	-2.71	1
Mg	24.3	-2.38	2
Al	26.9	-1.66	3
Fe	55.8	-0.44	2
Zn	65.4	-0.76	2
Cl_2	71.0	1.36	2
MnO_2	86.9	1.28	1
Li_xCoO_2	98	1.25	0.5

Table 5.1: Characteristics of typical electrode materials [1].

The cell voltage E^0 can be calculated as,

$$\text{Cell potential} = \text{Anode (oxidation)} + \text{Cathode (reduction)} \tag{5.2.2}$$

Therefore, for example, the standard cell potential of $Zn + Cl_2 \rightarrow ZnCl_2$ will be,

$$\text{Standard potential} = -(-0.76V) + 1.36V = 2.12V \tag{5.2.3}$$

Although the theoretical cell voltage is calculated in this manner, the practical voltage depends on some other factors such as temperature and conductivity of the electrode materials and electrolyte.

The theoretical capacity of a cell is a measure of the total quantity of electricity involved in the electrochemical reaction of the cell. It is determined by the amount of active material in the cell and defined in terms of Ah (ampere-hours). Theoretical capacity of a Zn/Cl_2 cell can be calculated by the equivalent mass of reactants. Theoretically, 1 gram equivalent mass of active material will deliver 26.8 Ah. Since two electrons are involved and the molecular mass is 65.4 of Zn, the electrochemical equivalent will be,

$$\text{Electrochemical equivalent of Zn} = \frac{65.4g}{26.8Ah \times 2} = 1.22g/Ah \qquad (5.2.4)$$

Similarly for the cathode (Cl_2), where molecular mass is 71.0g and electron involvement is 2, will be,

$$\text{Electrochemical equivalent of Cl} = \frac{71.0g}{26.8Ah \times 2} = 1.32g/Ah \qquad (5.2.5)$$

Therefore, the total theoretical capacity of a Zn/Cl will be,

$$1.22g/Ah + 1.32g/Ah = 2.54g/Ah \text{ or } 0.394Ah/g \qquad (5.2.6)$$

The energy of a battery is also related to the capacity. The voltage and the current of the battery are considered and the theoretical value is the maximum value that can be delivered by a system. For a Zn/Cl cell, from the calculated potential and the theoretical capacity, the specific energy can be calculated as follows,

$$\text{Specific energy} = 2.12V \times 0.394Ah/g = 835Wh/kg \qquad (5.2.7)$$

Although the above mentioned cell operations are general, there are a number of battery chemistries available today. A brief description of Lithium primary and Lithium-Ion secondary batteries is given in the following section as they are more related to the projects discussed in this thesis.

5.3 Lithium Primary Batteries

The term "lithium battery" refers to a family of different chemistries, comprising many types of cathodes and electrolytes along with a lithium anode. One of the main attractions of lithium as an anode material is its position as the most electropositive metal in the electrochemical series combined with its low mass, thus offering the largest amount of electrical energy per unit weight among all solid elements.

Lithium metal is very attractive in the battery industry because of its outstanding features such as light weight, being the lightest of all metallic elements, high voltage and good conductivity. Lithium is preferred to the other alkali metals because of its better mechanical characteristic and lower reactivity. Depending on the cathode material used, a lithium battery can have voltage up to about 4 V. This reduces the number of cells in a battery pack, compared to the typical 1.5V primary batteries. Many lithium batteries perform over a wide range of temperature 70 to -40 ˚C and some are designed to deliver high current and power levels. Lithium batteries also have a superior shelf life, i.e. those can be stored for a long period of time.

Nonaqueous solvents for electrolytes are used in lithium batteries. Water in any aqueous solution can react vigorously with lithium, releasing hydrogen and forming lithium hydroxide, very vigorous corrosive reaction with flammable hydrogen as the product.

$$2Li + 2H_2O \rightarrow 2LiOH + H_2 \tag{5.3.1}$$

Electrolyte based on organic solvents with sufficient stability and ionic conductivity such as EC (Ethylene carbonate) and PC (Propylene carbonate) or inorganic solvents such as thionyl-chloride ($SOCl_2$) are typically used. Ionic conductivity is induced by dissolving a suitable Lithium salt like $LiPF_6$ in an organic solvent. Lithium cells are generally properly sealed against contact with air and moisture.

Lithium primary batteries can be categorized into several types based upon the cathode and the electrolyte listed in Table 5.2:

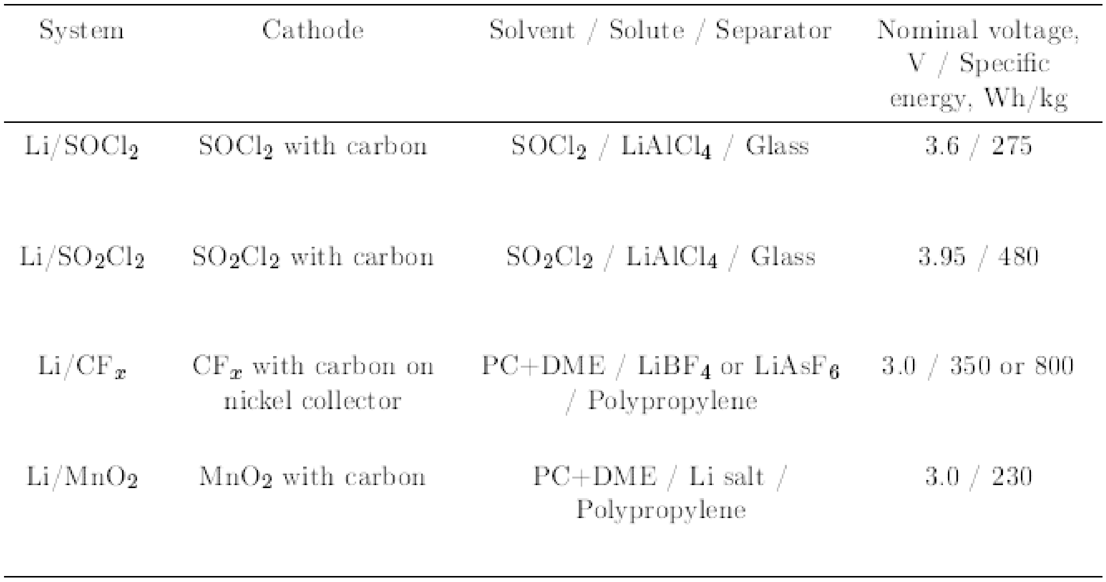

System	Cathode	Solvent / Solute / Separator	Nominal voltage, V / Specific energy, Wh/kg
Li/$SOCl_2$	$SOCl_2$ with carbon	$SOCl_2$ / $LiAlCl_4$ / Glass	3.6 / 275
Li/SO_2Cl_2	SO_2Cl_2 with carbon	SO_2Cl_2 / $LiAlCl_4$ / Glass	3.95 / 480
Li/CF_x	CF_x with carbon on nickel collector	PC+DME / $LiBF_4$ or $LiAsF_6$ / Polypropylene	3.0 / 350 or 800
Li/MnO_2	MnO_2 with carbon	PC+DME / Li salt / Polypropylene	3.0 / 230

Table 5.2: Characteristics of some Lithium primary batteries [1].

5.4 Lithium-Ion Batteries

A lithium-ion battery is a family of rechargeable battery types in which lithium ions move from the negative electrode to the positive electrode during discharge, and back when charging, but unlike lithium primary batteries, lithium-ion cells use an intercalated lithium compound as the electrode material instead of metallic lithium. Lithium-ion batteries were first commercialized in 1990 as a natural result of the extensive knowledge in intercalation chemistry accumulated by inorganic and solid state chemistry in the 1970s [2, 3]. The first generation of such batteries allowed storing more than twice the energy compared to nickel or lead batteries of the same size and mass [4].

Lithium ion batteries are available in wide variety of shapes and sizes efficiently fitting the device they power and much lighter than other comparable secondary batteries. Moreover, one of the major advantages is that no memory effect is associated with lithium-ion batteries. This kind of battery consists of two intercalation electrodes that can both host lithium ions as they are transferred on charge and discharge. Since no metallic lithium is present, the safety of the cells is immensely improved.

Depending on materials choices, the voltage, capacity, life, and safety of a lithium-ion battery can change dramatically. The anode of a conventional lithium-ion cell is made from carbonaceous materials. Carbon exhibits both electronic and ionic conductivity and can incorporate a large number of lithium ions. Their low cost, availability, low intercalation potential and good cycling properties have made them, so far, the most attractive anode choice for practical Li-ion cells. The most commercially popular anode material is graphite.

The cathode is a metal oxide usually a layered oxide (such as $LiCoO_2$), a polyanion (such as $LiFePO_4$), or a spinel (such as $LiMn_2O_4$) [5]. These materials are adhered to a metal foil current collector with a binder, typically PVDF (polyvinylidene fluoride). $LiCoO_2$ is the most commonly used cathode material in commercial Li-ion batteries today by virtue of its high working voltage, structural stability and long cycle life [6]. However, cobalt is an expensive metal and much effort has been made in recent years to find a cheaper alternative.

Li-ion batteries are assembled in their discharged state, with all lithium present in the positive electrode. During the first charge, carbonate-based electrolytes (solvents and salts) are reduced at the negative electrode (i.e. the carbon electrode). As a result, a surface film is formed consisting of a variety of solvent and salt reduction products. This film functions as an ionic conductor that allows Li^+ ions to be transported through the film during the subsequent intercalation and deintercalation processes. The film is also an electronic insulator, which will prevent the continuous reduction of electrolyte as the film thickness reaches a certain limit. This limit has been defined intuitively as the thickness at which electron tunneling from the graphite surface to the electrolyte is prevented (a few nm) [7]. The film then functions as a passivating layer on the graphite surface. It is most often referred to as a Solid Electrolyte Interphase (SEI). The interphase prevents further decomposition of the electrolyte after the second charge.

The choice of electrolyte is naturally one of the most important factors governing SEI layer formation, since different electrolyte species will be reduced to form different surface-film products. Liquid electrolytes in lithium-ion batteries consist of lithium salts, such as $LiPF_6$ or $LiBF_4$ in an organic solvent, such as ethylene carbonate (EC), dimethyl carbonate (DMC), and diethyl carbonate (DEC).

When a Li-ion cell is charged, the active positive electrode material is oxidized and the negative electrode is reduced. In other words lithium ions are de-intercalated from the positive electrode and intercalated into negative electrode through the electrolyte.

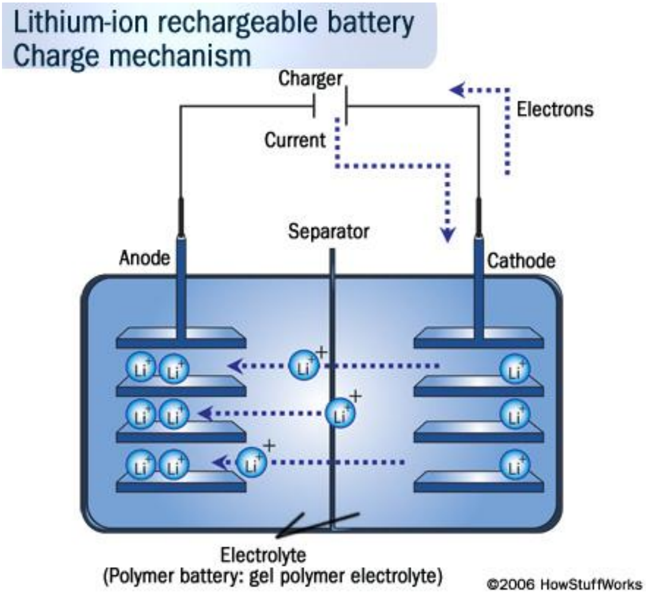

Figure 5.4.1: Li-ion Battery, charge mechanism

The reverse process occurs on discharge. Lithium ions are de-intercalated from the negative electrode and intercalated into the positive electrode through the electrolyte.

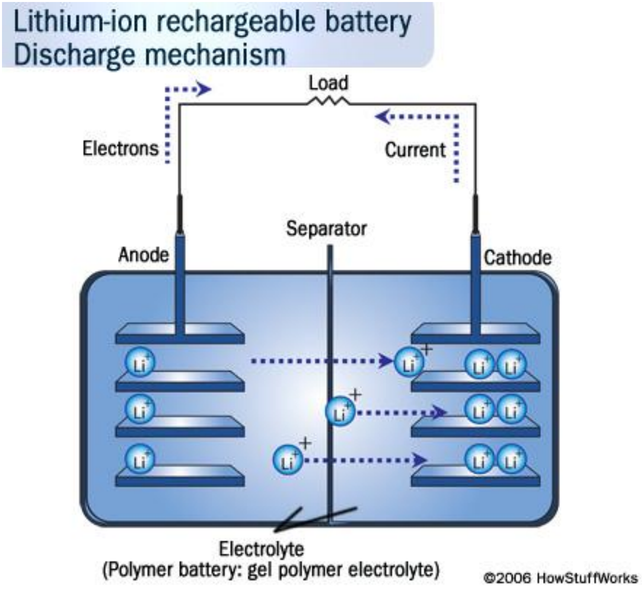

Figure 5.4.2: Li-ion Battery, discharge mechanism

However, these batteries still have serious drawbacks. Effects of prolonged cycling (repeated charge and discharge) or prolonged storage push them away from their theoretical and initially excellent performance [8-10]. These effects are typically capacity loss, poor cyclability, powder-fade and self-discharge.

Most of today's intercalation compounds have operating voltage between 4 and 4.5 V, and no major farther improvement should be expected. Intercalation compounds have limited capacity because the intercalation process is not an ideal energy storage mechanism. This situation occurs because of the limited number of vacancies available for lithium resulting in a limited utilization of the oxidation states of the host metal. An alternative process, *reversible conversion*, is described below.

Energy density is the product of the operating voltage and the capacity, and materials with very high operating voltage are known, but the stability window of the electrolyte constitutes a real limitation. Hence, high capacities hold the key to high energy density. Very large capacities can be obtained in *conversion reactions* because, unlike intercalation reactions, all of the oxidation states of the active material participate

[11]. Conversion Reaction is a relatively new reactivity concept with the reversible electrochemical reaction of lithium with transition metal oxides [12].

The overall reactions for *conversion reactions* are lithiation reactions in which the active material is fully reduced by lithium to the metal according to the following equation:

$$M^{z+}X_y + zLi \underset{\text{charge}}{\overset{\text{discharge}}{\rightleftarrows}} M^0 + yLi_{(z/y)}X \tag{5.4.1}$$

where M stands for a cation (transition metal) and X an anion (O^{-2}, S^{-2}, N^{-3} or F^{-}). As all the oxidation states of the material are utilized, capacities much higher than in the intercalation reactions currently used in rechargeable Li-ion batteries can in theory be obtained, thereby leading to much higher energy densities [13]**.**

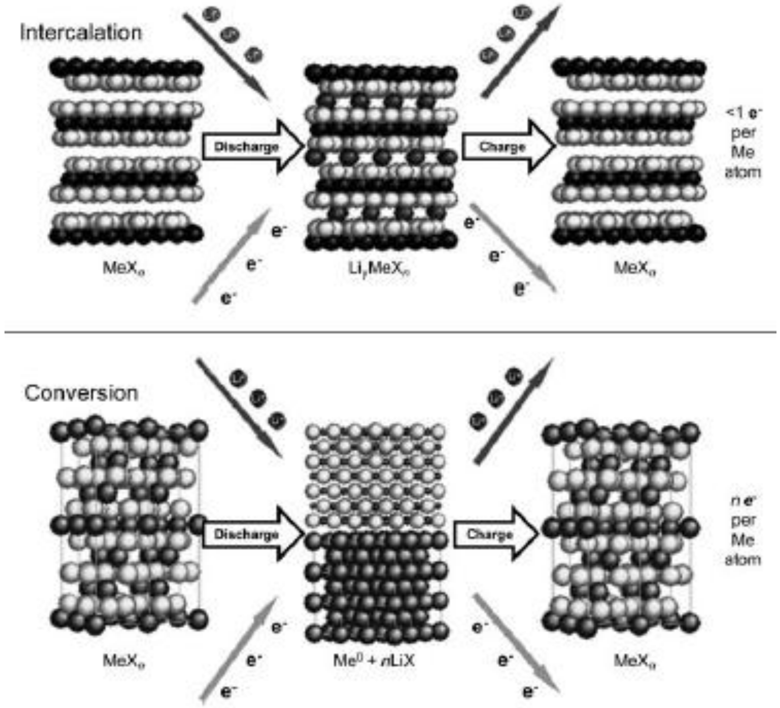

Figure 5.4.3: Illustration of the structural reconfigurations occurring during lithiation/delithiation via intercalation of a layered host material vs. that of a conversion reaction [14].

Conversion reactions have been known for a long time in primary battery applications with, for instance, the Li/CuO and Li/CF*x* systems that are still utilized today. Due to the highly destructive nature of the reaction, which literally involves the breaking of chemical bonds and the formation of new ones, it has long been thought that such reactions were irreversible. The earliest report on electrochemical reversible conversion reactions has been published by Besenhard in 1978 on non transition metals. It was shown that Bi_2S_3 was reduced into Bi^0 and Li_2S during lithiation (discharge) and was reoxidized with 75% efficiency during the following delithiation (charge); but this reversibility was observed for one cycle only [13].

The key to the reversibility of the conversion reaction seems to lie in the formation, upon complete reduction of the metal, of nanoparticles that, owing to the large amount of interfacial surface, are very active toward the decomposition of the matrix of the lithium binary compound (Li_nX) in which they are embedded when a reverse polarization is applied. The nanometric character of the metal particles has shown to be maintained even after several reduction-oxidation cycles [15].

For true conversion reaction, the cathode materials have to be ionic compounds such as metal halides. Metal fluorides have been shown to have appreciable reversible reactivity. It has been demonstrated that the electrochemical activity of high voltage/high energy density metal fluorides can truly be enabled when prepared in their nanostructured state and dispersed in a conductive matrix such as carbon or metal oxide. In Carbon Metal Fluoride Nanocomposites (CMFNC) the carbon matrix insures a high electronic conductivity while the metal fluoride nanoparticles present short diffusion pathways for the lithium and the possibility of electron tunneling. Other metal fluorides are capable of reversible conversion as well, for example, bismuth metal fluorides, such as BiF_3, which will be discussed in detail in the following chapters. Metal chlorides are not a practical solution because they are soluble in the electrolyte and are heavy, leaving metal fluorides as the only possible choice [13]. Metal oxyfluorides could in theory also be used for cathode application if they are cycled on the high-voltage fluorine conversion plateau [16].

Transition metal oxides are, by far, the family of compounds that react through conversion reactions deserving the most attention. Conversion reactions have not been observed for metals in groups 4 (Ti, Zr, Hf, and Rt) and 5 (V, Nb, Ta, and Db) [4].

Conversion compounds have also received attention for application as active materials at the anode side of the lithium battery, including metal nitride, sulfides, and oxide. They have low output voltage ranging from about 0.5 to about 1 V. In all of these compounds it has been demonstrated that the active material is reduced to the metal during lithiation with a parallel formation of the corresponding lithium compound. During the delithiation the reaction is reversed, the metal is reoxidized and returns to its original or slightly lower oxidation state. All the valence states of the cation of the active material are thus utilized in the reaction, thereby leading to high specific capacities.

Chapter 6

Nuclear Magnetic Resonance

6.1 Introduction

It was in December of 1945 when Purcell, Torrey and Pound detected weak signals generated by atomic nuclei in 1 kg of paraffin wax. Similar independent experiments performed by Bloch, Hansen and Packard observed radiofrequency signals generated from nuclei in water [1]. These series of experiments were the birth of the famous field known as Nuclear Magnetic Resonance (NMR).

Nuclear magnetic resonance is a spectroscopic technique that takes advantage of the interaction of nuclear spin with magnetic fields. NMR spectroscopy is one of the principal techniques used to obtain physical, chemical, electronic and structural information about molecules due to the chemical shift, Zeeman effect, the Knight shift effect, or quadrupole splittings on the resonant frequencies of the nuclei present in the sample. It is a powerful technique that can provide detailed information on the dynamics and three-dimensional structure of molecules in solution and in the solid state.

The science behind the NMR can be understood by classical physics or quantum physics. Consequently, a combination of both classical and quantum descriptions are used in the following section.

6.2 Spins and Magnetization

Spin **I** is a fundamental property of a nucleus like electrical charge or mass (and of course as spin is a previously described property of the electron). Some nuclei have integral spins and some others have half integral spins while yet other nuclei have no spin at all (Eg: ^{12}C, ^{16}O, ^{32}S).

When a magnetic field B_0 in **z** direction is applied to a nucleus with spin, the nucleus will tend to precess about the direction of the magnetic field (z-axis).

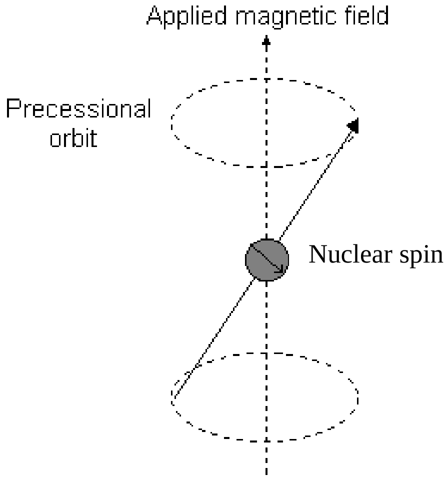

Figure 6.2.1: Spin precession around a constant magnetic field

The precession arises from the intrinsic nuclear magnetic moment $\boldsymbol{\mu}$. The combination of spin and charge generates the magnetic moment $\boldsymbol{\mu}$, and the nuclear magnetic moment and spin are related by the following equation [1]:

$$\boldsymbol{\mu} = \gamma \boldsymbol{I} \qquad (6.2.1)$$

where γ is the gyromagnetic ratio of the nucleus (which is specific for every nucleus, Table 6.1) and, $\boldsymbol{I}$ the net nuclear spin.

Nuclei	Net Spin	γ(MHz/T)
^{1}H	1/2	42.58
^{2}H	1	6.54
^{31}P	1/2	17.25
^{3}Na	3/2	11.27
^{14}N	1	3.08
^{13}C	1/2	10.71
^{19}F	1/2	40.08
^{7}Li	3/2	10.40

Table 6.1: Gyromagnetic ratios of some commonly used isotopes [2]

The magnetic moment $\boldsymbol{\mu}$ can have any orientation in space, but in an external magnetic field it aligns itself in such way as to minimize the energy of the system, given by:

$$E = - \mu \cdot B_0 = - \mu_z B_0 = - \gamma I_z B_0 \tag{6.2.2}$$

The quantization rule for I_z is:

$$I_z = m\hbar \tag{6.2.3}$$

where m can take the values $m = I, I\text{-}1, \ldots, -I$ and I is the nuclear spin angular momentum.

There are $(2I+1)$ possible values for I_z and therefore the same number of energy levels. Hence, the energy of the system is:

$$E = - \mu \cdot B_0 = - \mu_z B_0 = - m\gamma\hbar B_0 \tag{6.2.4}$$

The energy difference between two consecutive energy levels is:

$$\Delta E = \gamma\hbar B_0 \tag{6.2.5}$$

which consequently is the minimum energy the system can absorb or emit.

The magnetic field B_0 will cause the nucleus to precess about the z-axis at a frequency $\nu = \omega_0 / 2\pi$, where ω_0 is called the *Larmor frequency*, given by:

$$\omega_0 = \gamma B_0 \tag{6.2.6}$$

The precession is clockwise for $\gamma > 0$ or counterclockwise for $\gamma < 0$. Hence, energy transitions between the energy levels of the system involve absorption or emission of photons of energy ΔE [1], given by:

$$\Delta E = h\nu = \hbar\omega \tag{6.2.7}$$

So far, only a single nucleus in a magnetic field has been considered, however to analyze the behavior of a collection of nuclei it is necessary to use statistical analysis. Applying Boltzman statistics to a simple two state system where $I = 1/2$, and $m = 1/2$, -1/2 results in:

$$\frac{N_\beta}{N_\alpha} = e^{-\frac{\Delta E}{K_B T}} \approx 1 - \frac{\Delta E}{k_B T} = 1 - \frac{\gamma \hbar B_0}{k_B T} \tag{6.2.8}$$

where N_β is the number of nuclei in the highest energy level, N_α is the number of nuclei in the lowest energy level and, k_B is the Boltzmann constant. Generally, the population difference in a material at typical NMR magnetic fields and ambient temperature is approximately 10^{-6}.

The collective behavior of the spins in matter can be visualized in the following manner. If the material is divided into small domains, each of the domains will have a net magnetization that is the vector sum of all the spins in that domain. The domain magnetization will randomly fluctuate in time, but the net magnetization of the material will be zero over time. If this material is introduced into a magnetic field, there will be a small excess of the domain[1] magnetizations that will align themselves parallel to the magnetic field at any instant in time. The result is a net magnetization of the material in the direction of magnetic field B_0 (z direction). This is called the material's equilibrium magnetization vector (M_0).

---

[1] not to be confused with ferromagnetic domains.

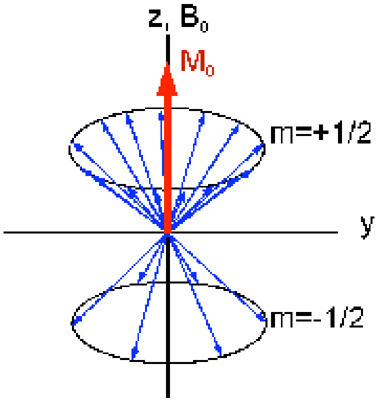

Figure 6.2.2: Net magnetization vector M_0

Using this coordinate system (the laboratory frame), the total magnetization in the z direction (M_z) is equal to M_0, and the magnetization in the x and y directions (M_x, M_y) are zero.

In order to simplify the mathematics it is convenient to define a coordinate system as one that rotates around B_0 (z-axis) at the frequency ω_0 (Larmor frequency), this is known as the *rotating frame*. Let's consider two reference frames, i.e. a fixed reference frame (or laboratory frame), with axes e_x, e_y, e_z, and a rotating reference frame, with axes denoted e'_x, e'_y, e'_z rotating with an angular velocity ω. The frame axes are related as:

$$\begin{aligned} e'_x &= e_x \cos\omega t + e_y \sin\omega t \\ e'_y &= e_y \cos\omega t - e_x \sin\omega t \\ e'_z &= e_z \end{aligned} \tag{6.2.9}$$

One standing and watching a rotating vector **F**:

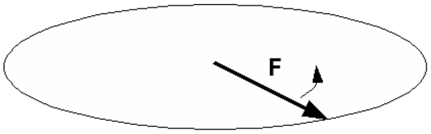

Figure 6.2.3: Rotation of vector **F**.

The vector, **F**, rotates with angular velocity ω and, the motion of **F** in the laboratory frame is described by:

$$dF/dt = \omega \times F \tag{6.2.10}$$

Note that d/dt is used for the laboratory frame and $\partial/\partial t$ for the rotating frame. If we jump on to the rotating frame and look at the vector **F** again, it will appear to be motionless with $\partial F/\partial t = 0$.

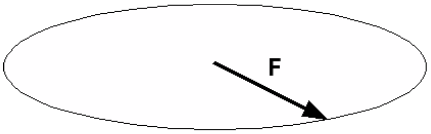

Figure 6.2.4: Motionless vector **F**.

Now, we suppose that there is a vector, **G**, that appears motionless in the laboratory frame: $dG/dt = 0$. From the rotating frame, which is rotating at angular frequency ω, it will appear to us to be rotating with angular frequency $-\omega$: $\partial G/\partial t = -\omega \times G$.

Looking at vector **G** from the rotating frame but this time **G** is moving in both the laboratory frame and the rotating frame, it will have its $-\omega$ movement plus the laboratory frame movement: $\partial G/\partial t = -\omega \times G.+ dG/dt$, or $\partial G/\partial t = G \times \omega + dG/dt$.

This is the general transformation equation from laboratory to rotating frame coordinates. A magnetization vector rotating at the Larmor frequency in the laboratory frame appears stationary in a frame of reference rotating about the z-axis.

At this point, if a coil is used to produce a resonant oscillating magnetic field B_1 perpendicular to B_0 in the xy-plane, M_0 will move away from the z direction, and resulting in a net M_x and M_y magnetizations. B_1 is applied in the form of radio frequency (RF) pulses with resonance frequency ω, described by $B_1 = B_1 \cos(\omega t)\mathbf{i} + B_1 \sin(\omega t)\mathbf{j}$. Then it can be shown that the effective magnetic field B_{eff} in the rotational frame will be,

$$B_{eff} = B_{rf}\,\mathbf{i} + (B_0 - \omega/\gamma)\mathbf{k} \qquad (6.2.11)$$

If the applied RF pulse is matched with the Lamor frequency, i.e $\omega = \omega_0$, the effective magnetic field can be considered as a static field introduced along the x-axis. The RF flips the magnetic moment off of the z-axis with an angle depending on the length τ of the pulse applied:

$$\theta = \gamma B_1 \tau \tag{6.2.12}$$

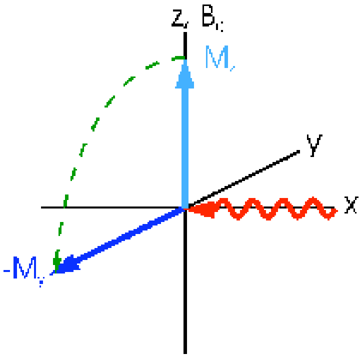

Figure 6.2.5: Effect of B_1 on the magnetization vector

M_z could be reduced to zero by applying an RF pulse that rotates the magnetization vector by 90° onto the x-y plane. This is called a 90° pulse. The net magnetization in the x-y plane is called the *transverse magnetization*.

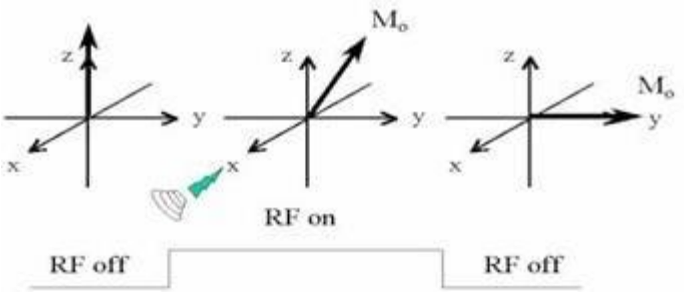

Figure 6.2.6: Effect on the net magnetization by a 90° RF pulse

Shortly after a material is subjected to these conditions, it will emit radiation mainly in the form of an RF signal. The RF signal is received by the coil on the NMR probe and spectroscopically processed to extract information about the material in question. This time scaled signal is called FID or *Free Induction Decay*. Fourier transformed FID gives us a frequency spectrum which contains information including chemical shifts, different interactions such as dipolar, quadrupolar coupling about the sample as shown in the figure below.

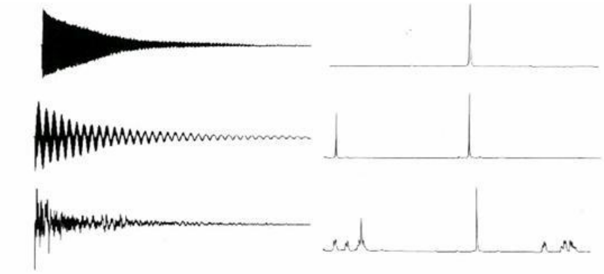

Figure 6.2.7: NMR FIDs and their Fourier transformed spectra

The behavior of the magnetization vector as it returns to equilibrium can be described semi-classically by the Bloch equations [3], Eqn. (6.2.13), which are the equations of motion for the nuclear spin magnetization in the rotating frame.

$$\begin{aligned}\frac{dM_x(t)}{dt} &= \gamma(\mathbf{M}(t)\times\mathbf{B}(t))_x - \frac{M_x(t)}{T_2}\\ \frac{dM_y(t)}{dt} &= \gamma(\mathbf{M}(t)\times\mathbf{B}(t))_y - \frac{M_y(t)}{T_2}\\ \frac{dM_z(t)}{dt} &= \gamma(\mathbf{M}(t)\times\mathbf{B}(t))_z - \frac{M_z(t)-M_0}{T_1}\end{aligned} \tag{6.2.13}$$

where **M** is the magnetization vector and **B** is the magnetic field.

After an RF pulse is applied, the magnetization vector relaxes to its initial state along B_0 in the z-axis. This relaxation process is called the *spin-lattice relaxation* and it is characterized by a time T_1. Only the z-component of the magnetization is affected by this phenomenon. The analytic solution the spin-lattice relaxation can be obtained from the Bloch equation for M_z:

$$\frac{dM_z}{dt} = -\frac{(M_z(t)-M_0)}{T_1} \tag{6.2.14}$$

The solution of equation (6.2.14) is:

$$M_z(t) = M_z(\mathbf{0})\left(1 - e^{-\frac{t}{T_1}}\right) \tag{6.2.15}$$

In the x-y plane the magnetization is affected by the presence of local field inhomogeneities. This causes each of the spin domains to experience a slightly different magnetic field. Therefore, the spin domains precess at different Larmor frequencies and start to dephase. This process is called *spin-spin relaxation* and is characterized by a time T_2. The analytic solution of the spin-spin relaxation process can be obtained from the Bloch equations for M_x and M_y.

$$dM_x / dt = -\omega[(M_y - M_x(t)) / T_2]$$

$$dM_y / dt = -\omega[(M_x - M_y(t)) / T_2] \qquad (6.2.16)$$

where $\omega = 2\pi v$. The solutions for these equations are:

$$M_x(t) = M_0 \cos(\omega t) \exp\{-t/T_2\}$$

$$M_y(t) = M_0 \sin(\omega t) \exp\{-t/T_2\} \qquad (6.2.17)$$

where M_0 is the magnitude of the spin magnetization. It should be mentioned that $T_2 \leq T_1$ and although these two processes have been discussed separately, they actually occur simultaneously.

There are two main processes that contribute to the decay of the transverse magnetization: molecular interactions and differences in the magnetic fields affecting by the spin domains (inhomogeneous T_2 processes). The combination of these two effects is denoted T_2^*:

$$1/T_2^* = 1/T_2 + 1/T_{2\text{inhomogeneous}} \qquad (6.2.18)$$

In any condensed phase, a nuclear spin experiences a great number of interactions. They can be categorized as external and internal interactions. External interactions, Zeeman and RF were already discussed in the previous section. Major internal spin interactions/Hamiltonians in solids will be discussed next.

6.3 Chemical Shift

Chemical shift is one of the most important features of the NMR spectrum. It might be expected that each nuclear isotope gives us a single narrow peak in the frequency scale corresponding to their Lamor frequency. However, this is not so because of slight variation of magnetic field that each nucleus experiences. These variations are usually caused by electron current in the molecular orbitals, and in some cases unpaired electron spin. The electron distribution of a particular nucleus (e.g. ^{1}H, ^{13}C, ^{15}N) varies according to the local environment (binding partners, bond lengths, angles between bonds, etc), and with it the local magnetic field at each nucleus. Therefore, the electronic environments of an atom shields or de-shields it from the external magnetic field resulting in a somewhat different local magnetic field at each nucleus. Different atoms with different local electronic environments "feel" a different external field and resonate at different frequencies. This variation of nuclear magnetic resonance frequencies of the same kind of nucleus, due to variations in the electron distribution, is called the *chemical shift*.

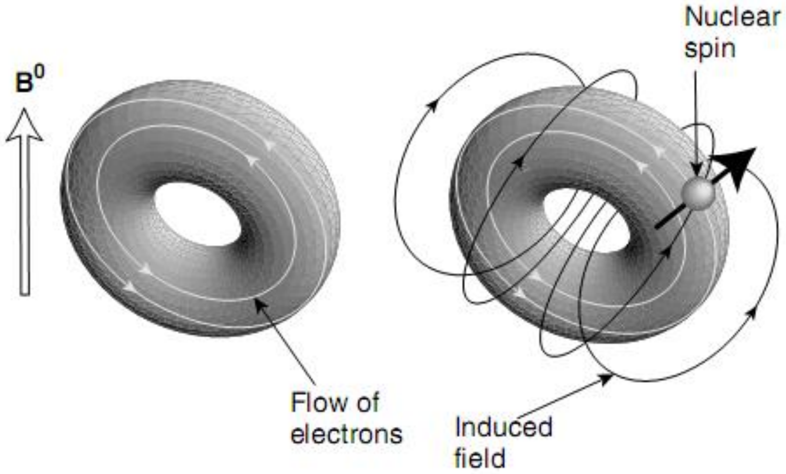

Figure 6.3.1: Mechanism of the Chemical Shift.

The size of the chemical shift is given with respect to a reference frequency or reference sample, usually a molecule with a barely distorted electron distribution. Chemical shift is denoted by δ and the unit is *ppm* (parts per million). The chemical shift is defined by:

$$\delta = \frac{\nu - \nu_{ref}}{\nu_{ref}} \tag{6.3.1}$$

where v is the spectral frequency of the signal for the spin of interest, and v_{ref} is the resonance frequency of the same spin in some reference compound.

The chemical shift Hamiltonian acting on a spin **I** is:

$$H_{cs} = -\gamma\hbar \mathbf{I}\, \sigma\, B_0 \tag{6.3.2}$$

where B_0 is the applied magnetic field, σ is a second-rank tensor called the chemical shift tensor [4].

The chemical shift can be considered as a sort of fingerprint for each atom, which plays an important role in NMR spectroscopy to reveal the aspects of an atom in its particular geometry and bonding configuration. The value of the chemical shift may depend upon the orientation of the molecule with respect to the magnetic field, an important consideration in solids.

6.4 Dipole-Dipole Coupling

Each nuclear spin is a magnet and generates a magnetic field in the surrounding space according to the direction of the spin magnetic moment (Fig. 6.4.1). A second nuclear spin may interact with the field and vice-versa. This mutual interaction is called *dipole-dipole coupling*.

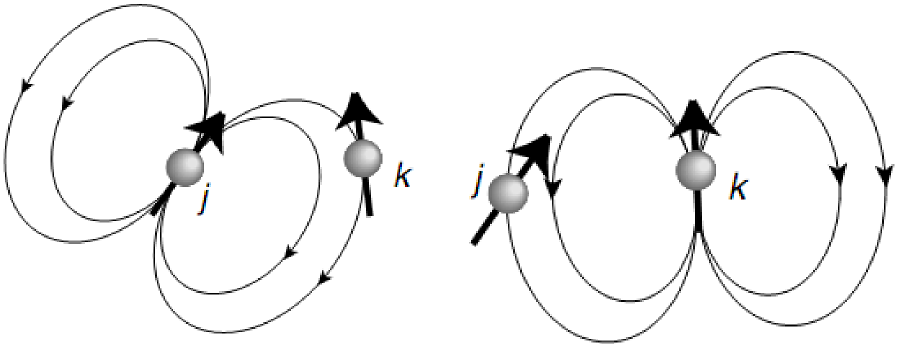

Figure 6.4.1: Magnetic loops generated by spin j (left) and spin k (right)

The dipole-dipole coupling can be intermolecular or intramolecular. The full form the dipole-dipole interaction Hamiltonian between spin I_j and I_k is represented as,

$$\boldsymbol{H}_{jk} = -\frac{\mu_0}{4\pi}\frac{\gamma_j\gamma_k}{r_{jk}^3}\left(3\left(\boldsymbol{I}_j.\boldsymbol{e}_{jk}\right)\left(\boldsymbol{I}_k.\boldsymbol{e}_{jk}\right) - \boldsymbol{I}_j.\boldsymbol{I}_k\right) \tag{6.4.1}$$

where e_{jk} is a unit vector parallel to the line joining the centers of the two nuclei (Fig. 6.4.2), γ_j and γ_k are the gyromagnetic ratios of the two spins, and r_{jk} is the distance between the two spins.

Dipole-dipole coupling is very useful in structural studies as it depends only on known physical constants and the inverse cube of the inter-nuclear distance.

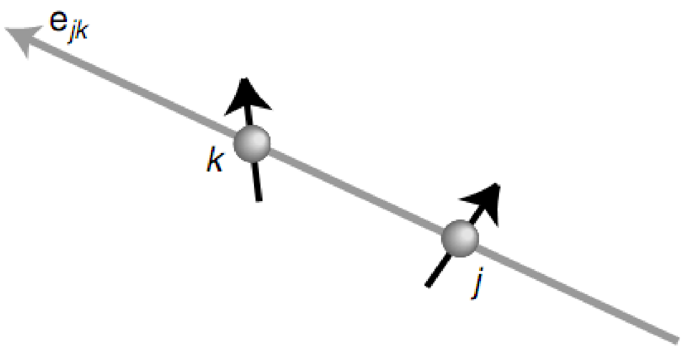

Figure 6.4.2: Unit vector parallel to the line joining the centers of the two spins.

6.5 Quadrupolar Coupling

Nuclei with a spin angular momentum quantum number greater than 1/2 are called quadrupolar nuclei because these nuclei possess, in addition to their magnetic dipole moment, an electric quadrupole moment.

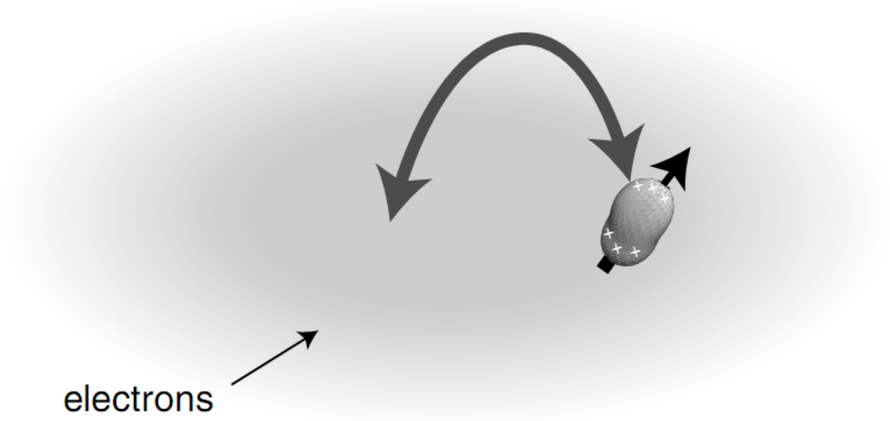

Figure 6.5.1: Surrounding electric gradient field

Electric quadrupole moments may couple to their surrounding electric field gradient, which for a nucleus arises from asymmetric bonding environments. Quite often, this electric quadrupolar coupling is much stronger (i.e. in energy) than the magnetic couplings to neighboring nuclei. The effect of such strong quadrupolar couplings on the NMR spectrum significantly decreases the NMR sensitivity and resolution. If the quadupolar interaction is much smaller than the Zeeman interaction, the secular quadrupolar interaction of spin I_j is given by,

$$\boldsymbol{H}_j \cong \omega_j \left(3\boldsymbol{I}_{jz}^2 - \boldsymbol{I}_j.\boldsymbol{I}_j\right) \tag{6.5.1}$$

where ω_j is called the *quadrupolar frequency* and for solids is given by,

$$\omega_j = \frac{3eQ_j}{4I_j\left(2I_j - 1\right)} V_{j,zz} \tag{6.5.2}$$

here Q_j is the electric *quadrupole moment* of the nucleus, *e* is the charge of the proton and $V_{j,zz}$ is the component of the electric field gradient at the nucleus I_j .

6.6 Single Pulse Experiment

This is one of the simplest and most basic experiments in NMR. The pulse sequence used is called *single pulse sequence*. An RF pulse is applied to the sample. The magnetization flips off of the z-axis (B_0 field direction). The proper pulse width and amplitude will rotate the magnetization down to the xy-plane.

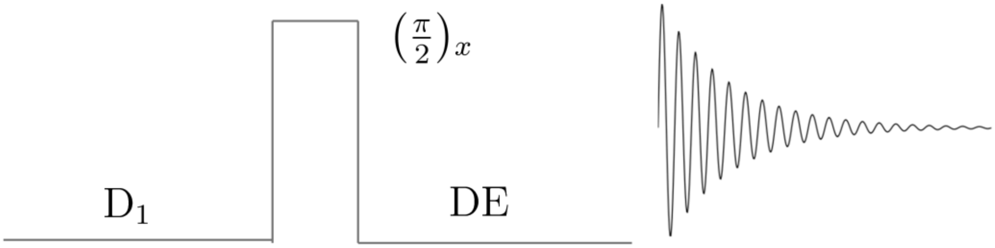

Figure 6.6.1: Single Pulse

The interpulse delay (relaxation delay) D_1 serves to allow the spin system to relax back towards equilibrium. This is important for achieving the maximum signal-to-noise ratio. If the spin system doesn't relax sufficiently (called *saturation*) the relative intensity of the observed NMR peaks will suffer. The longer the relaxation delay, the closer the spin system returns to equilibrium. A long relaxation delay means a long experiment; therefore some type of compromise is made in practice. D_1 is typically set to about 5 times T_1.

The dead time, DE, is a short delay between the end of the pulse and the beginning of acquisition. This is needed for the electronics of the system to stabilize following the high power RF pulse.

6.7 Spin Echo Experiment

The spin echo is one of the most fundamental building blocks for NMR pulse sequences. Its main purpose is to refocus the magnetization, remove the signal from the dead time, and minimize the probe background signal.

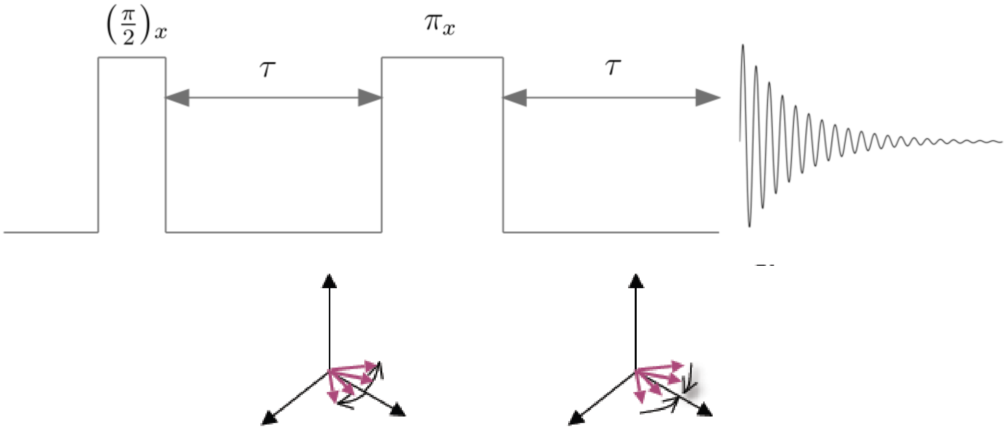

Figure 6.7.1: Spin-Echo pulse sequence

The first pulse $(\pi/2)_x$ is applied along the +x-axis and rotates the magnetization vector by 90° degrees from the +z-axis to the –y-axis of the rotating frame. During the first delay period τ, the magnetization rotates in the xy plane and the spins dephase by a combination of local or external magnetic field inhomogeneities. Other effects such as spin-spin interactions or intermolecular interactions may contribute significantly to the spin dephasing. After the dephasing time τ, a second pulse $(\pi)_x$ is applied along the +x-axis. This pulse rotates the dephased spins by 180° degrees, effectively reversing the dephasing process. At a time τ after the second pulse, the spins refocus and an echo is formed.

6.8 Magic Angle Spinning (MAS) NMR

The main three NMR interactions in solids we have discussed, dipolar, chemical shift anisotropy and quadrupolar coupling often lead to very broad and featureless spectra. In liquids most of these interactions will average out because of the rapid time-averaged molecular motion that occurs. MAS (*Magic Angle Spinning*) is a powerful technique that averages these interactions described by second-rank tensor by spinning the sample at the *magic angle* ($\theta = 54.74°$) with respect to the direction of the magnetic field. The normally broad lines become narrower, increasing the resolution for better identification and analysis of the spectrum.

Each interaction mentioned above has a dependence on the second-order Legendre polynomial, $P_2(\cos\theta) = (3\cos^2\theta - 1)$. That means, if θ is chosen to be 54.74° (the magic angle), the expression $(3\cos^2\theta - 1)$ becomes equal to zero and the interactions are averaged to zero or reduced to the isotropic values.

In order for the MAS method to be successful, spinning has to occur at a rate equal to or greater than the dipolar linewidth (which can be many kHz wide). Samples are finely powdered and packed tightly into rotors, which are then spun at rates from 1 to 70 kHz, depending on the rotor size and type of experiment being conducted. If the sample is spun at a rate less than the magnitude of the anisotropic interaction, a manifold of spinning sidebands becomes visible, which are separated by the rate of spinning (in Hz).

The *nuclear dipole-dipole interactions* between magnetic moments of nuclei average to zero only at a specific angle. Non-secular[2] parts of the Hamiltonian (Eq. 6.4.1) can be discarded in high magnetic field and the remaining secular part can be divided into two parts depending on the two spins whether they are homo-nuclear or hetero-nuclear. Homo-nuclear part is given by,

---

[2] Terms that do not commute with Zeeman Hamiltonian.

$$H_{homo} = d_{jk} (3I_{jk} I_{kz} – I_j I_k) \tag{6.8.1}$$

and the hetero-nuclear part is,

$$H_{hetero} = d_{jk}2I_{jz}I_{kz} \tag{6.8.2}$$

Here, d_{jk} is known as *secular dipole-dipole* coupling and given by,

$$d_{jk} = b_{jk}1/2(3\cos^2\theta_{jk} – 1) \tag{6.8.3}$$

θ_{jk} is the angle between e_{jk} and the external magnetic field e_z. The coupling constant b_{jk} depends on the distance between spins and the orientation. There is a solution to Eqn. (6.8.3) that makes d_{jk} zero and hence H_{homo} and H_{hetero} become zero.

$$3\cos^2\theta_{jk} – 1 = 0 \tag{6.8.4}$$

That solution of Eqn. (6.8.3) is called the *Magic Angle*, that is 54.74^0.

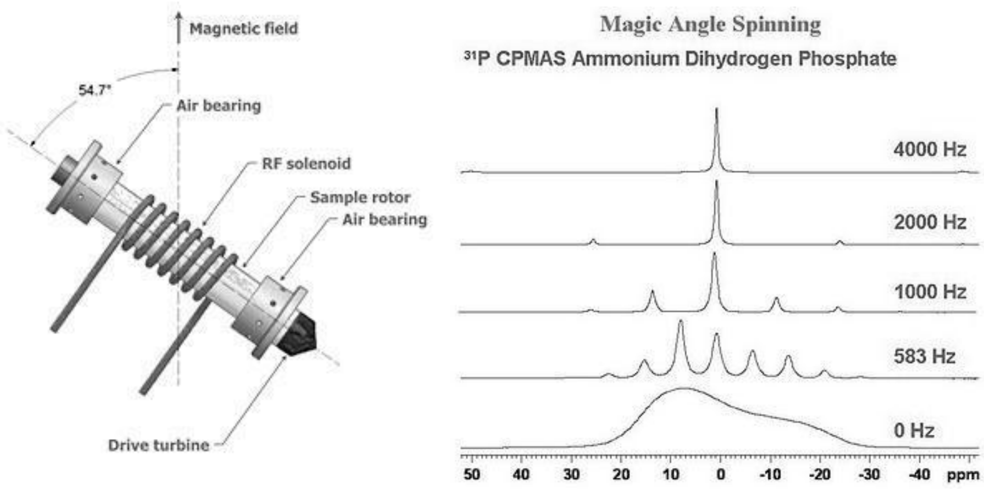

Figure 6.8.1: MAS spinning setup (left), MAS spectra (right)

The *chemical shift anisotropy* averages to a non-zero value called the isotropic chemical shift under MAS, producing high resolution NMR spectra. When spinning the sample at low speed the chemical shift anisotropy will result in spinning sidebands, as shown in Fig. 6.8.1.

At high enough speed the spinning sidebands get smaller, and the spectrum consists of narrow lines at the isotropic shifts.

In order to describe the MAS NMR experiment more qualitatively, the chemical shift affects the NMR frequency, which is determined by the Zeeman interaction between a nuclear magnetic moment μ and the external static magnetic field B_0. The chemical shift Hamiltonian in the rotating frame is written as:

$$H_{CS} = \{\sigma_{iso}\gamma B_0 + ½\, \delta[3\cos^2\theta - 1 - \eta\sin^2\theta\cos(2\varphi)]\}I_z \qquad (6.8.5)$$

The chemical shift and its anisotropy are represented by a tensor σ that is most conveniently represented in the coordinate system in which it is diagonal. This is in the principal axis system (PAS), which is an axis frame defined in such a way that the symmetric part of the shielding tensor is diagonal, and the principal values of the shielding tensor can be given as:

$$\sigma_{iso} = 1/3(\sigma^{PAS}{}_{xx} + \sigma^{PAS}{}_{yy} + \sigma^{PAS}{}_{zz})$$
$$\delta = \sigma^{PAS}{}_{zz} - \sigma_{iso}$$
$$\eta = (\sigma^{PAS}{}_{xx} - \sigma^{PAS}{}_{yy}) / \delta \qquad (6.8.6)$$

Here, σ_{iso} is the isotropic value, δ is the anisotropy, and η is the asymmetry parameter. The dependence on the molecular orientation in Eq. (6.8.5) is of the form $(3\cos^2\theta - 1)$, where θ is the angle that describes the orientation of the spin interaction tensor, which is chemical shift tensor in case of the chemical shift interaction. Only the term $\sigma_{iso}\gamma B_0$ in Eq. (6.8.5) remains and high resolution spectra are obtained in solid state.

The *Quadrupolar coupling* is only partially averaged by MAS (first order) leaving a residual second order quadrupolar interaction, but that is often good enough to achieve satisfactory spectral resolution. First-order quadrupolar coupling depends on the orientation of the interaction tensor with the external magnetic field, does not affect the central transition and, can be removed by MAS. The quadrupolar interaction can be described as a perturbation of Zeeman interaction, first-order quadrupolar Hamiltonian expression is:

$$H_Q^{(1)} = 1/2Q'(\theta,\varphi)[I_z^2 - I(I + 1)/3] \qquad (6.8.7)$$

where $Q'(\theta,\varphi) = (\omega_Q/2)[3\cos^2\theta - 1 - \eta\sin^2\theta\cos2\varphi]$ is the quadrupolar splitting, and $\omega_Q = 3e^2qQ/[2I(2I - 1)\hbar]$ the quadrupole frequency, with θ and φ as polar angles. eQ is the magnitude of the nuclear electric quadrupole moment, eq the magnitude of the electric field gradient (denoted as V in eq. 6.5.2), e the charge on the electron, I the spin quantum number of the nucleus, and η the asymmetry parameter, where $0 \leq \eta \leq 1$. If $\eta = 0$, the electric field gradient (EFG) tensor is axially symmetric.

The averaging is only close to zero in a first-order perturbation theory treatment; higher order terms cause allowed frequencies at multiples of the spinning frequency to appear, creating spinning side-bands in the spectra. The magic angle is a root of the second-order Legendre polynomial, $P_2(\cos\theta) = 0$, so the first-order quadrupolar interaction vanishes at the magic angle as in the case of dipolar interactions. In some cases there is a substantial second-order effect of the quadrupole coupling that broadens even the central transition.

In order to achieve high resolution, the angle must be set very precisely. This is commonly done by looking at the ^{79}Br signal of KBr (potassium bromide). The intensity of the spinning sidebands for the satellite transition of ^{79}Br is strongly related to the precision of the magic angle. The sidebands appear as rotational echoes in the ^{79}Br FID or *free induction decay*. The more rotational echoes the stronger the sidebands and therefore the more precise the angle setting. Although any quadrupolar isotope with strong satellite transition sidebands can be used for this purpose, the ^{79}Br of KBr is particularly convenient as the resonance is very close to ^{13}C, has a short T_1, and can be seen easily in one scan.

Chapter 7

ELECTROLYTE SOLUTION

7.1 Introduction

It has become increasingly important in today's society to have ready access to energy in different forms. Rechargeable batteries are therefore becoming immensely important, by virtue of their ability to store electricity and make energy mobile [1]. New markets are being created for these batteries, notably for the purpose of powering portable electronics, and EV/HEV's. Lithium ion (Li-ion) battery fulfils many of these demands.

Li-ion batteries are assembled in their discharged state, with all lithium present in the positive electrode. During the first charge, carbonate-based electrolytes (solvents and salts) are reduced at the negative electrode (i.e. the carbon electrode) at a potential between ca. 1.5-0.7 V vs. Li/Li^+ (i.e. prior to any lithium intercalation), depending on the composition of the electrolyte [2]. As a result, a surface film is formed consisting of a variety of solvent and salt reduction products. This film functions as an ionic conductor that allows Li^+ ions to be transported through the film during the subsequent intercalation and deintercalation processes. The film is also an electronic insulator, which will prevent the continuous reduction of electrolyte as the film thickness reaches a certain limit. This limit has been defined intuitively as the thickness at which electron tunneling from the graphite surface to the electrolyte is prevented (a few nm) [3]. The film then functions as a passivating layer on the graphite surface. It is most often referred to as a Solid Electrolyte Interphase (SEI). Surface films formed on lithium metal and carbon electrodes are very similar [4].

The choice of electrolyte is naturally one of the most important factors governing SEI layer formation, since different electrolyte species will be reduced to form different surface-film products. The primary requirements of the reduction products in a functional SEI layer are Li^+ ion conductivity and electronic insulation. This is one of the major reasons why alkyl carbonates are the preferred choice of solvent. Their reduction products are mainly inorganic or semi-organic lithium carbonates. This superiority, as suggested by Gan et. al., may be due to orbital interaction and conjugated charges in the CO_3- group, which will provide an efficient mechanism for Li^+ on conduction through the SEI [5]. The SEI layer composition is also highly dependent on impurities in the cells.

An oxygen-17 NMR study has been employed to assess the degree of preferential solvation of Li^+ ions in binary mixtures of EC (ethylene carbonate) and DMC (dimethyl carbonate) containing $LiPF_6$ (lithium hexafluorophosphate) which may be ultimately related to the SEI formation mechanism.

7.1.1 Electrolyte

An electrolyte is any substance containing free ions that make the substance electrically conductive. The most typical electrolyte is an ionic solution, but molten electrolytes and solid electrolytes are also possible. Commonly, electrolytes are solutions of acids, bases, or salts.

Electrolyte solutions are normally formed when a salt is placed into a solvent such as water and the individual components dissociate due to the thermodynamic interactions between solvent and solute molecules, in a process called solvation. If a high proportion of the solute dissociates to form free ions, the electrolyte is strong; if most of the solute does not dissociate, the electrolyte is weak.

Electrolytes are ubiquitous and indispensable in all electrochemical devices, the role of electrolytes in batteries is to serve as the medium for the transfer of ions between a pair of electrodes. The vast majority of the electrolytes consist of salts (also called "electrolyte solutes") dissolved in solvents, either water (aqueous) or organic molecules (nonaqueous), and are in a liquid state in the service-temperature range. Because of its physical location in the electrochemical devices, that is, being sandwiched between positive and negative electrodes, the electrolyte is in close interaction with both electrodes; therefore, when new electrode materials come into use, the need for compatible electrolytes usually arises. The interfaces between the electrolyte and the two electrodes often dictate the performance of the devices.

In a battery, the chemical nature of positive and negative electrodes decides the energy output, while the electrolyte, in most situations, determines to some extent how fast the energy could be released by controlling the rate of mass flow within the battery. Conceptually, the electrolyte should undergo no net chemical changes during the operation of the battery, and all Faradaic processes are expected to occur within the electrodes. Therefore, in a somewhat oversimplified description, an electrolyte could be viewed as the inert component in the battery, and it must demonstrate stability against both cathode and anode surfaces [6].

The stability of an electrolyte can also be quantified by the range in volts between its oxidative and reductive decomposition limits, which is known as the “electrochemical window”. Obviously, the redox potential of both electrode materials must fall within this electrochemical window to enable a rechargeable battery operation. An electrolyte should include the following minimal requirements [7]:

(1) It should be a good ionic conductor and electronic insulator, so that ion transport can be facile and self-discharge can be kept to a minimum.

(2) It should have a wide electrochemical window, so that electrolyte degradation would not occur within the range of the working potentials of both the cathode and the anode.

(3) It should also be inert to other cell components such as cell separators, electrode substrates, and cell packaging materials.

(4) It should be robust against various abuses, such as electrical, mechanical, or thermal ones.

(5) Its components should be environmentally friendly.

In order to achieve higher performance of the batteries, high ionic conductivity for the non-aqueous electrolyte solution is indispensable. The ionic conductivity depends not only on the ion transport properties, but also on ion pair formation of the component anions. At a molecular level, however, understanding of the physical properties of non-aqueous electrolyte solutions currently utilized for the lithium ion secondary batteries is still limited [8]. On the other hand, it is well known that the ion pair formation between the oppositely charged ions in solution strongly depends on the solvent property (not only the ion-solvent interaction, but also solvent-solvent interaction) [9]. Therefore, it is necessary to study the ion-ion, the ion-solvent and the solvent-solvent interactions in non-aqueous electrolyte solutions at a molecular level.

Most compositions of lithium electrolytes are based on solutions of one or more lithium salts in mixtures of two or more solvents. The rationale behind this mixed solvent formulation is that the diverse and often contradicting requirements of battery applications can hardly be met by any individual compound, for example, high fluidity versus high dielectric constant; therefore, solvents of very different physical and chemical natures are often used together to perform various functions simultaneously. A mixture of salts, on the other hand, is usually not used, because anion choice is usually limited, and performance advantages or improvements are not readily demonstrated.

7.1.2 Solvents

Liquid solvents that fulfill the dual requirements of a high lithium ion conductivity (>10^{-3} S/cm), and a broad electrochemical stability window are mainly carbonates, ethers and esters of various kinds. The carbonates are by far the most common choice under ambient conditions, because of their superior cycling behavior.

An ideal electrolyte solvent should meet the following minimal criteria [7]:

(1) It should be able to dissolve salts to sufficient concentration. In other words, it should have a high dielectric constant (ϵ).

(2) It should be fluid (low viscosity η), so that facile ion transport can occur.

(3) After the SEI is formed and the electrolyte is stable it should remain inert to all cell components, especially the charged surfaces of the cathode and the anode, during cell operation.

(4) It should remain liquid in a wide temperature range. In other words, its melting point (T_m) should be low and its boiling point (T_b) high.

(5) It should also be safe (high flash point T_f), nontoxic, and economical.

The nonaqueous compounds that qualify as electrolyte solvents must be able to dissolve sufficient amounts of lithium salt; therefore, only those with polar groups such as carbonyl (C=O), nitrile (C≡N), sulfonyl (S=O), and ether-linkage (-O-) merit consideration. Since the inception of nonaqueous electrolytes, a wide spectrum of polar solvents has been investigated, and the majority of them fall into either one of the following families: organic esters and ethers.

While all of the ethers, cyclic or acyclic, demonstrate similar moderate dielectric constants and low viscosities, cyclic and acyclic esters behave like two entirely different kinds of compounds in terms of dielectric constant and viscosity; that is, all cyclic esters are uniformly polar and rather viscous, and all acyclic esters are weakly polar and fluid. The origin for the effect of molecular cyclicity on the dielectric constant has been attributed to the intramolecular strain of the cyclic structures that favors the conformation of better alignment of molecular dipoles, while the more flexible and open structure of linear carbonates results in the mutual cancellation of these dipoles [7]. Cyclic diesters of carbonic acid have high dielectric constant and, hence, their ability to dissolve a wide variety of lithium salts.

The compatibility between different solvents is determined by two factors:

(1) molecular structure similarity and

(2) melting point proximity [10].

A solvent with an ideal electrochemical stability for a high-energy-density battery purpose should possess high oxidation and low reduction potentials at the same time. The state-of-the-art electrolytes use mixtures of cyclic and acyclic carbonates as solvents, whose functions are to solvate lithium salts and to facilitate lithium ion transport.

The key cyclic solvent, EC (ethylene carbonate), is also responsible for forming a protective SEI on graphitic anodes and a surface layer on metal oxide cathodes as well. However, this indispensable solvent simultaneously sets the narrow range of service temperature for these electrolytes with its high melting point, while its replacement by other low-melting solvents such as its structural analogue PC (polycarbonate) is often rendered difficult by the requirement for SEI-forming ability.

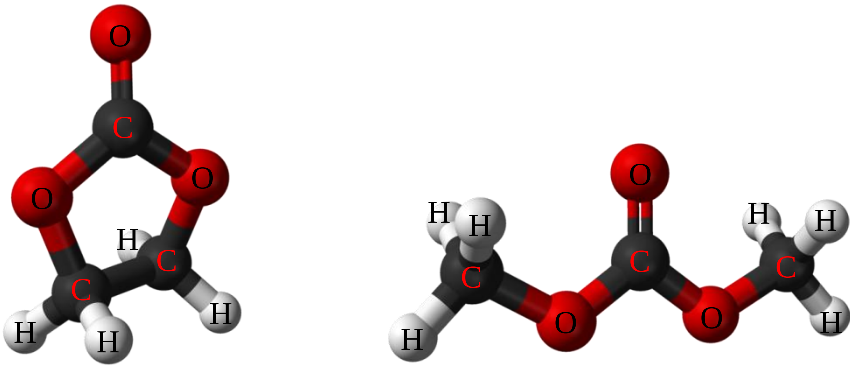

Figure 7.2.1.1: EC and DMC

On the other hand, the linear carbonates used in the state-of-the art electrolytes, DMC, DEC, and EMC, serve as diluents to the high-melting and viscous EC. They have been known to be unsuitable as single solvents because of their inability to solvate lithium salts as well as their instability on the oxidizing surface of cathode materials, while the out-gassing of lithium ion cells during long-term cycling is also believed to arise from them [7].

Carbonates and esters are more anodically stable, while ethers are more resistant to cathodic decompositions.

EC became the core and indispensable component of the electrolyte formulation. Efforts were made to expand the limited liquid range of EC-based electrolytes by using different cosolvents. Tarascon and Guyomard reported using a linear carbonate, dimethyl carbonate (DMC), as a cosolvent with EC [11, 12]. As it has been pointed out, linear carbonates differ from their cyclic cousins by their low boiling points, low viscosity, and low dielectric constant. They can form homogeneous mixtures with EC at any ratio, and the resultant mixed electrolytes benefit not only from the melting-temperature suppression of EC but also from the low viscosity (higher ion conductivity) of DMC. But what surprises researchers is the wide electrochemical stability window of this mixture electrolyte: it remains stable on a spinel cathode surface up to 5.0 V [7].

It seems that a synergistic effect is achieved when EC and DMC (or other linear carbonates) are mixed because the merits of each individual solvent are imparted on to the resultant mixture: high anodic stability of EC on cathode surfaces, high solvation power of EC toward lithium salts, and low viscosity of DMC to promote ion transport. For our experiments EC and DMC were used as the solvents.

7.1.3 Salt

Soluble lithium salts are added to the solvents to act as charge carrier during the electrochemical process. Good stability and charge separation of anion and cation are needed to obtain this high conductivity. This is normally achieved by choosing bulky anions with low negative charge density [13]. Examples of salts are $LiClO_4$, $LiAsF_6$, $LiPF_6$, $LiBF_4$, LiF_3SO_3 and $LiN(SO_2CF_3)_2$.

The salt most commonly used in commercial cells is lithium hexafluorophosphate, $LiPF_6$. It is an inorganic compound, with low moisture, high purity and, high solubility in nonpolar solvents. The highly purity grade of $LiPF_6$ has the characteristics of low free acid and high solubility, and it should be handled in a dry environment. This salt is extremely hygroscopic and may evolve volatile fluorides such as POF_3 and HF as products of decomposition if allowed to be in contact with moisture.

HF is a highly reactive impurity that reacts readily with carbonates [13-15]. The presence of LiF on the electrode surfaces results from $LiPF_6$ instablility. LiF is, contrary to lithium carbonates, an unwanted SEI component, because of its low permeability for Li^+ ions (low Li^+ ion conductivity).

$LiPF_6$ gives high ionic conductivities in carbonate-based solutions, and shows excellent cycling properties at room temperature. It is known, however, to show poor thermal stability [16-19] and poor cycling behavior for some electrode materials at slightly elevated temperature [17, 20], and is highly sensitive to hydrolysis by trace water.

The instability of $LiPF_6$ could be another driving force for surface film formation. The hydrolysis of the $LiPF_6$ molecule results in LiF and $Li_xPF_yO_z$ compounds, which are observed on all electrodes. If PF_5 is formed in large amounts from $LiPF_6$ decomposition, it can act to some extent as an initiator for EC polymerization. Zhang et. al. reported that decomposition of $LiPF_6$, according to:

$$LiPF_6 \leftrightarrow LiF + PF_5 \tag{7.1.3.1}$$

increases markedly above room temperature, and that reactions between PF_5 and solvents produce some polymeric species [19].

The morphology and thickness of the SEI are also major factors to consider for a salt. A thicker SEI replacing the electrolyte in the space between the electrode particles results in a longer diffusion path through the SEI layer. For $LiPF_6$ containing system, the thermal instability of the SEI layer leading to formation of LiF, removal of carbonates, and increase in polymeric hydrocarbons are all detrimental effects, which depend on the salt instability or, more specifically, on anion type [7].

In nonaqueous solvents based on mixed alkyl carbonates, $LiPF_6$ remains one of the most conducting salts. For example, in EC/DMC (1:1) the conductivity is 10.7 mS cm-1 [7]. This excellent conductivity results from the combination of its ionic mobility and dissociation constant. The solution of $LiPF_6$ in mixed carbonates can effectively resist oxidation up to 5.1 V [21, 22], thus making it one of the few salts that can actually support the operation of 4.0 V cathode materials.

EC as the solvent and $LiPF_6$ as the solute with one or more linear carbonates, selected from DMC, DEC, or EMC, are also used as cosolvents to increase the fluidity and reduce the melting point of the electrolyte, thus forming the popular composition consisting of $LiPF_6$/EC/linear carbonate(s). However, certain restrictions on battery performance arise from these state-of-the-art electrolytes, for which these two indispensable components are mainly responsible:

(1) a low-temperature limit (-20 °C) set by EC due to the high melting point and the high liquidus temperature it confers upon the solvent mixture, and

(2) a high-temperature limit (60 °C) set by $LiPF_6$ due to its reactivity with solvents. As a result, the commercialized lithium ion batteries can only deliver their rated capacity and power in the temperature range -20 to 60 °C.

However, $LiPF_6$/EC/DMC electrolytes are very stable at room temperature in the proper containers, and a more efficient and protective SEI formed by the $LiPF_6$-based electrolyte reveals $LiPF_6$ as the favored salt in electrolytes, because it forms a smoother and more uniform SEI, thus minimizing the probability of dendrite growth on a relative scale as compared with the cases of the other salts studied [7].

7.2 Oxygen-17 NMR

Of the three naturally occurring oxygen isotopes (^{16}O, ^{17}O and ^{18}O), only ^{17}O possesses a nuclear spin (I = 5/2). Oxygen-17 NMR has a low sensitivity and very low natural abundance 0.037 %, presents wide chemical shifts range (up to 2000 ppm), and cation affinity (especially in the carbonyl position) which makes it a sensitive probe of ion solvation effects. Also, it suffers from low sensitivity due to the large quadrupolar interactions of ^{17}O spins, which result in broad lines. Therefore, it is one of the most difficult nuclei to observe by NMR spectroscopy presenting a technical challenge to facile data collection.

^{17}O is however of great interest to use as a nucleus because is located at strategic molecular sites and is directly involved in inter- and intra-molecular interactions. The ^{17}O NMR parameters, i.e., isotropic shielding, principal elements of the ^{17}O shielding and electric field gradient tensors, and transverse and longitudinal relaxation times can be considered as excellent means for probing structure, bonding and dynamics of oxygen containing compounds. ^{17}O NMR may provide structural and dynamic information which is difficult or impossible to obtain using other techniques.

Changes in chemical shift can potentially be used to monitor conformational changes, substrate binding, changes in the hydrogen-bonding and protonation state of the molecule studied.

The molecular mobility of solvent molecules and ions in liquid electrolytes has two aspects, i.e. translation mobility and rotational mobility. Both of these types of mobility are very important for NMR, because they tend to average out many of the nuclear spin interactions.

Unlike the complicated NMR spectra of quadrupolar nuclei in the solid state, the spectra in solution are quite simple as all of the energy levels are equally spaced by the Zeeman interaction, the first and second order quadrupolar effects averaged by the rapid isotropic motion in solution. However quadrupolar effects usually enhance the relaxation of nuclear spins in isotropic liquids. If the molecular rotation is relatively slow the secular quadrupolar Hamiltonian is a poor approximation and would need the second-order correction [23].

In order to overcome the problem of low sensitivity, one should use as much sample as possible either as a neat liquid (if the sample is a liquid) or in a very concentrated solution with a solvent free of oxygen (if the sample is a solid). There may also be problems if the quadrupolar interaction dominated relaxation rate is too fast resulting in resonances that are very broad.

7.3 Experimental

The objective was to study ^{17}O NMR of an electrolyte solution ($LiPF_6$) with binary solvents mixtures, in particular EC and DMC. Electrolyte samples with different ratios of solvents were packed in a 10 mm sample tubes in the Argon glovebox for avoidance of moisture and air contamination. The 10 mm tubes probe provides about twice the sensitivity over the 5 mm probes and consequently better signal-to-noise ratio. Quartz tubes were used as opposed to borosilicate glass because the electrolytes become reactive at higher temperatures.

The ^{17}O NMR spectra were recorded on a Bruker DPX 400 spectrometer at 54.25 MHz, and the sample temperature was set at 323º K to reduce the sample viscosity and hence spectral linewidth. H_2O was used as reference set to 0 ppm

Typical electrolyte solutions were prepared by dissolving calculated amount of $LiPF_6$ in pre-mixed solvents consisting of varying ratios of EC, and DMC. No co-solvent was added because that will compete with the carbonates for association with the Li^+ ions, which is the purpose in this study.

Observation of very broad resonances in ^{17}O NMR is a serious problem due to baseline distortions. The most severe origin of baseline artifacts is the transient response of the NMR probe, often referred to as ‘‘acoustic ringing”, caused by the generation of ultrasonic waves from the action of the rf pulse [24, 25]. The most commonly used method of avoiding baseline distortions has been the insertion of a sufficiently long delay time, Δt, between the end of the pulse and the beginning of data acquisition. Multipulse sequences have the advantage that they can be applied in a routine way and they do not require modification of probe design. For experiments in solution, the Ring Down Elimination (RIDE) pulse sequence [26-27] is quite effective in eliminating acoustic responses. The Ring Down Elimination (RIDE) pulse sequence is the following:

$$
\begin{gathered}
90_x - \Delta t - FID^{(+)} - 180_x - t - 90_x - \Delta t - FID^{(-)} \\
90_{-x} - \Delta t - FID^{(-)} - 180_x - t - 90_{-x} - \Delta t - FID^{(+)} \qquad (7.3.1)
\end{gathered}
$$

where (±) denotes addition or subtraction of the data.

7.4 Results and Discussion

Upon dissolution in the binary solvent mixture to form the electrolyte, the Li^+ ions, from the $LiPF_6$ salt, are solvated and stabilized to different extents by EC and DMC. Due to the positively charged nature of the Li cation, one would expect that the carbonyl oxygen of each carbonate species would preferentially interact with the cation during solvation simply because it has greater electron density and is more electronegative than its ether counterpart. Consequently, any observations of ^{17}O chemical shift changes between the pure carbonate mixture and the $LiPF_6$/EC/DMC mixture would be directly attributable to solvation interactions between the carbonates and Li^+ [28].

Figure 7.4.1 displays the ^{17}O chemical shifts of the binary mixture post 1.0M $LiPF_6$ addition relative to the chemical shifts of the binary mixture and *Figure 7.4.2* shows the ^{17}O shifts of a 50-50 mixture relative to the shifts for pure EC and pure DMC. The data compiled in figures 7.4.1 and 7.4.2 were consistent with our expectations, with the carbonyl oxygen atoms of EC and DMC being further downfield than their corresponding ether oxygen atoms [29].

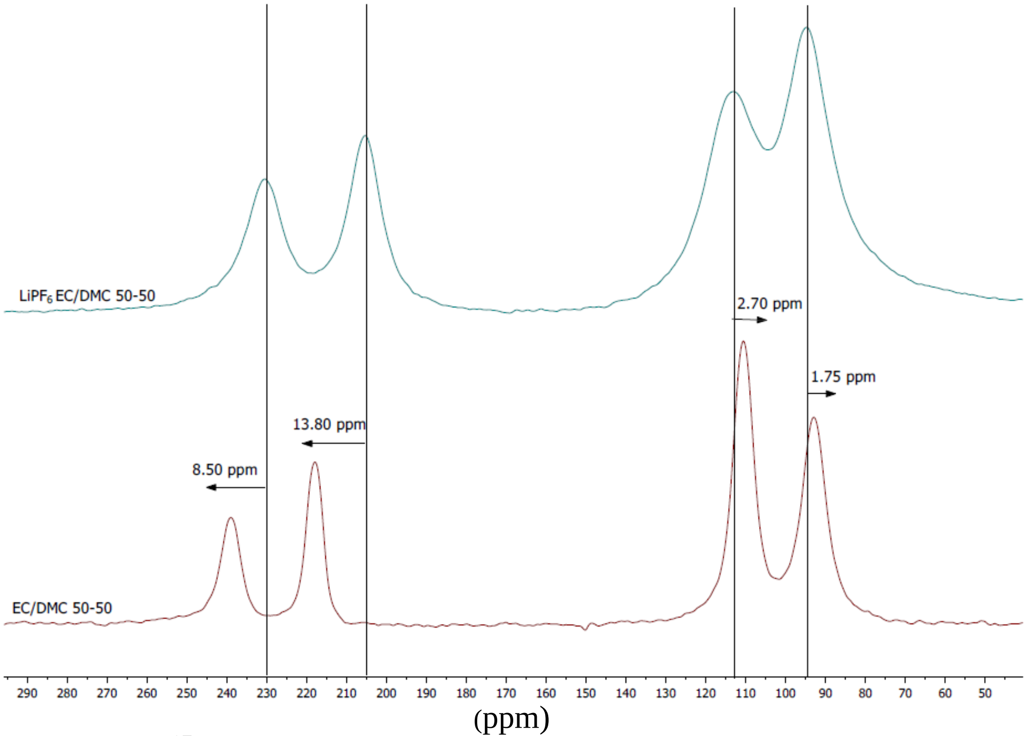

Figure 7.4.1: ^{17}O NMR spectrum of a 50-50 EC/DMC mixture overlaid with the spectrum of a 50-50 binary mixture containing 1M $LiPF_6$.

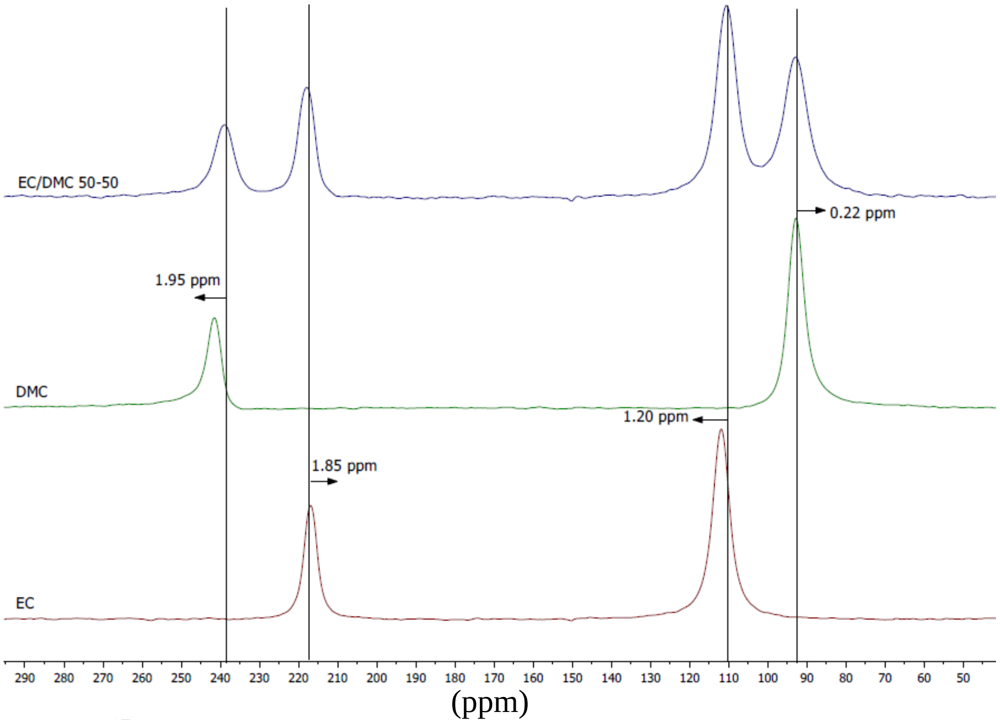

Figure 7.4.2: ^{17}O NMR spectrum of a 50-50 EC/DMC mixture overlaid with spectra of pure EC and pure DMC.

It should be pointed out that in Figs. 7.4.1 and 7.4.2, the absolute values of the chemical shifts were plotted instead of the actual values because the actual values are negative, denoting an upfield chemical shift, and it might prove misleading to conceptualize a larger negative number as being a bigger shift than a smaller negative number i.e. a shift of -20 ppm would be a bigger shift than a -10 ppm shift.

Figure 7.4.3 details the changes between the differences in the ^{17}O chemical shift of the carbonyl groups associated with eleven different solutions. The ratios of the co-solvents EC and DMC are varied across solutions such that each successive mixture contains ten percent more EC and ten percent less DMC by molar ratio. The concentration of the LiPF$_6$ salt was however, maintained at a constant 1M in each solution.

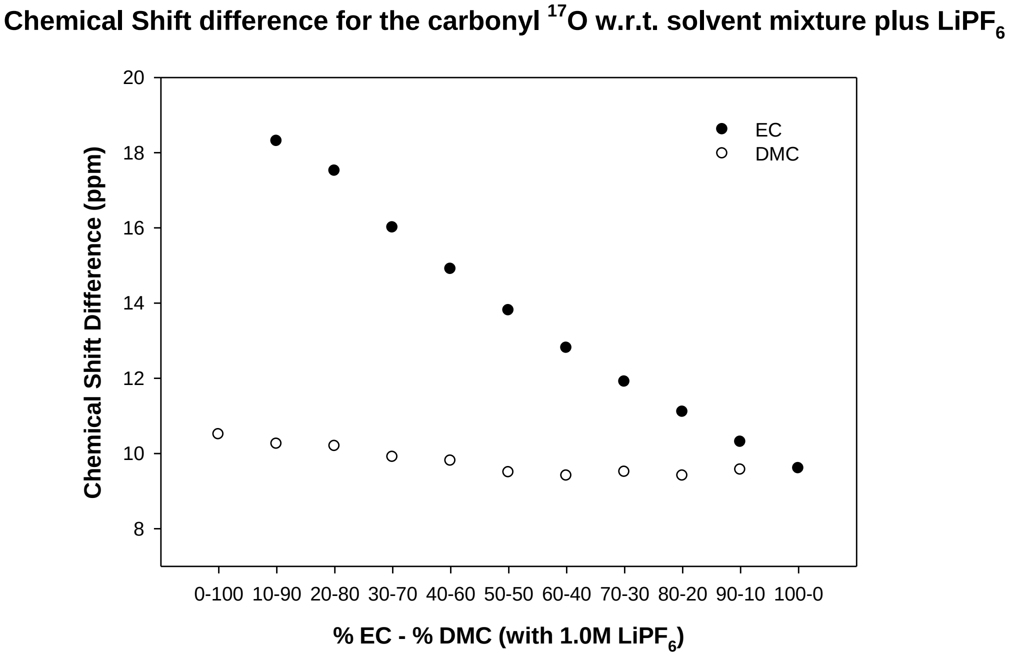

Figure 7.4.3: Absolute chemical shift differences with respect to solvent mixture composition for the carbonyl oxygen atom.

Figure 7.4.4 details the changes between the differences in the ^{17}O chemical shift of the ether groups associated with eleven different solutions.

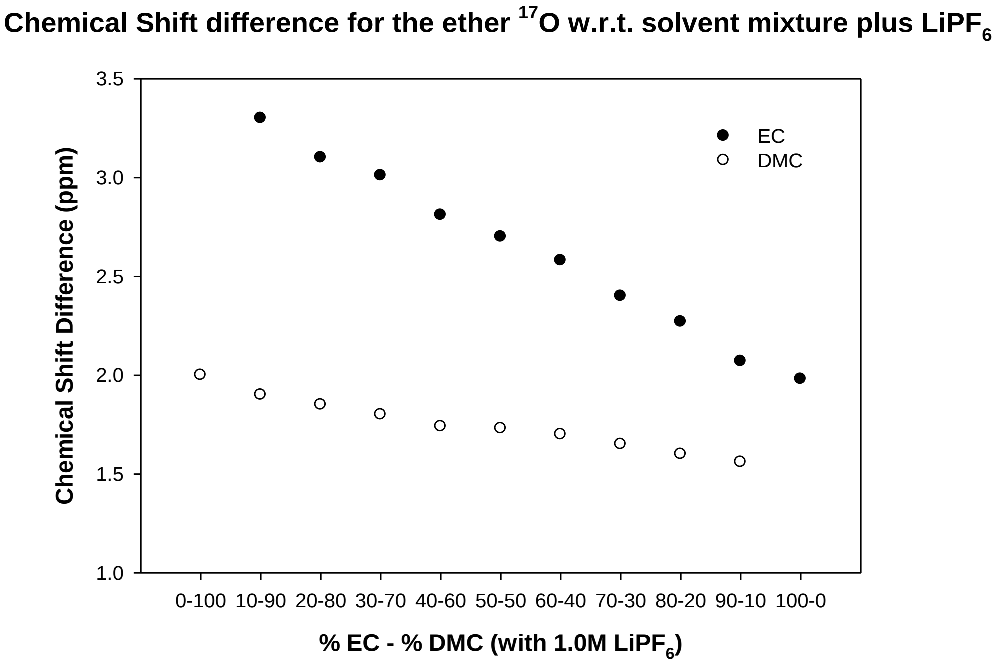

Figure 7.4.4: Absolute chemical shift differences with respect to solvent mixture composition for the ether oxygen atom.

The Li^+ cation exhibits a higher affinity for EC than for DMC because of its higher solvent dipole [30]. This is supported by the data presented in Figs. 7.4.3 and 7.4.4. In both cases, the chemical shifts associated with the oxygen resonances of EC are substantially larger than those of DMC. This strongly supports preferential association of Li^+ to EC because larger chemical shift changes are indicative of greater changes in the electronic environment of the nucleus being observed (^{17}O). The carbonyl ^{17}O resonances of both EC and DMC show upfield shifts which are consistent with the oxygen nucleus becoming more shielded [29]. Preferential association of Li^+ to the carbonyl intramolecularly, serves to rationalize why the shifts for the carbonyl oxygen are larger than those for the ether oxygen which are the result of an indirect, inductive effect [31].

Interestingly, in figures 7.4.3 and 7.4.4, the largest chemical shift differences for EC are observed for the 10:90 EC/DMC mixtures. This chemical shift subsequently decreases with increasing EC concentration. This observation is consistent for both carbonyl and ether oxygen atoms. This can be explained by taking into account what happens on a molecular level and as Lucht et. al. showed, changes in the chemical shift are caused primarily by the Li^+ cations being associated to the carbonates via the carbonyl oxygen atoms [32].

On the NMR timescale, the carbonyl oxygen resonance that we observe for EC in the EC/DMC/1.0M $LiPF_6$ mixture, represents an average signal of all EC molecules present. This implies that the ratio of associated to unassociated EC molecules determines the chemical shift for this resonance. Given that the concentration of $LiPF_6$ is constant in all the mixtures, then the ratio of associated to unassociated EC molecules is highest for the “10-90” binary mixture. However, as the concentration of EC increases from sample to sample, then the ratio decreases and consequently, the observed chemical shift also decreases. This accounts for the constant decrease observed in the ^{17}O chemical shift for the carbonyl upon going from the “10-90” mixture (18.3 ppm) to the “100-0” mixture (9.6ppm). A similar explanation is given for the shifts observed for the ether oxygen of EC the only difference being that the shifts are smaller as they are caused by an indirect inductive effect rather than a direct association of Li^+.

Figures 7.4.5 and *7.4.6* illustrates the effect of simply mixing the solvents together on the ^{17}O chemical shift. The chemical shift differences that are observed are computed relative to the shifts of the pure carbonates. These shifts are fairly common and are typically attributed to Van der Waal interactions, magnetic anisotropy or polar attractions between the solvent molecules being mixed together [33].

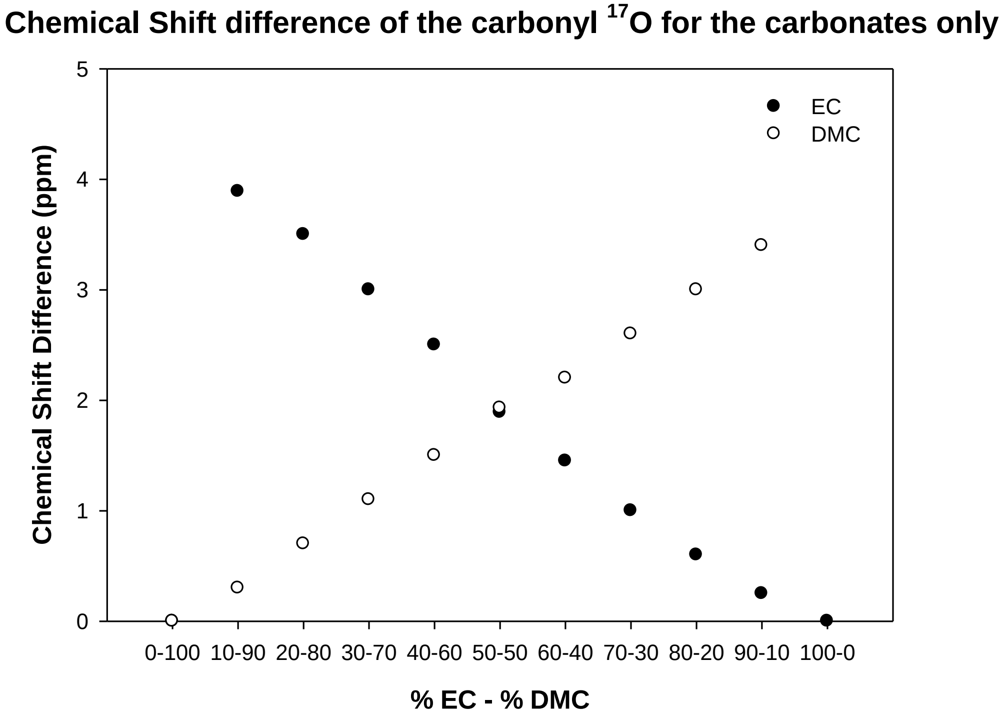

Figure 7.4.5: Chemical shift differences of the binary mixture of the solvents for the carbonyl oxygen atom without $LiPF_6$.

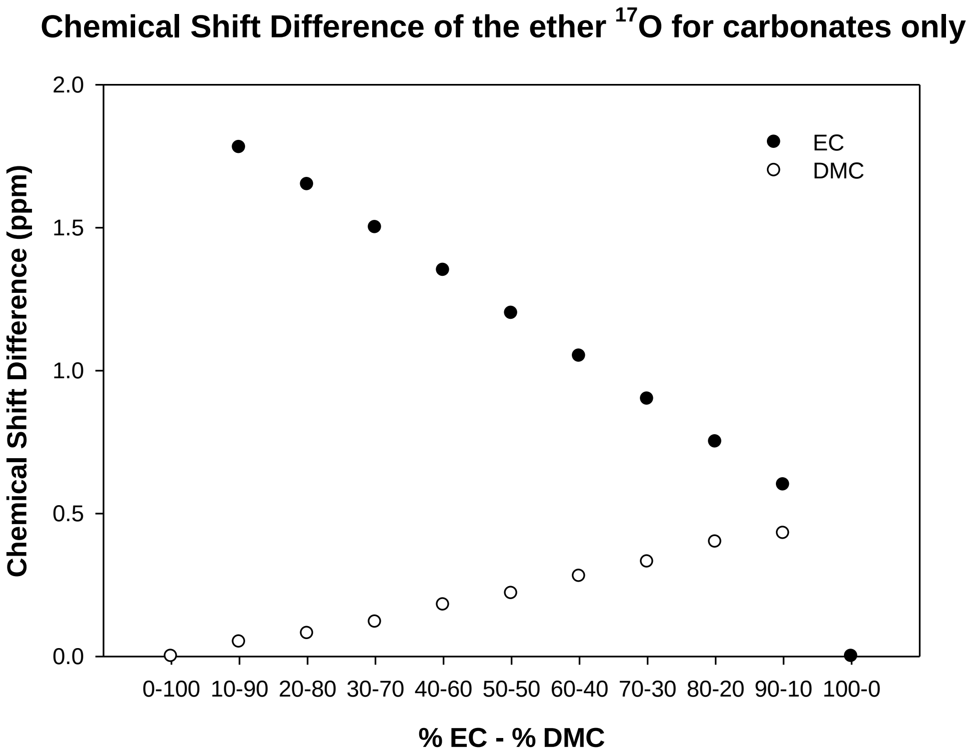

Figure 7.4.6: Chemical shift differences of the binary mixture of the solvents for the ether oxygen atom without $LiPF_6$.

7.5 Conclusion

A recent investigation of solvation preference has been carried out using "soft" electrospray ionization mass spectrometry, in which it was found that the primary solvation sheath of Li^+ ions consists largely of the cyclic carbonate even when the cyclic/acyclic carbonate ratio in the starting solution is relatively low [30].

Lucht and coworkers employed a ^{13}C study to probe a similar EC/DMC/DEC $LiPF_6$ electrolyte solvent system and concluded that of the three carbonates, EC preferentially binds to Li+ ions in the electrolyte [32]. This conclusion was reached based on the observation that the largest ^{13}C chemical shifts of the carbonyl resonance was observed for that corresponding to the carbonyl of EC. Furthermore, the shift of this resonance was also observed to change with both variations in the concentration of the $LiPF_6$ salt as well as changes in temperature. The carbonyl resonances of DMC and DEC displayed significantly smaller shifts with respect to salt concentration and showed almost no variation with temperature.

In this work it is shown that the largest effect of the solute on the ^{17}O chemical shift is observed at the carbonyl oxygen, with a strong preference for Li^+ association with EC over DMC, in line with expectations of solvent preference from previously cited studies [30-32]. Because the oxygen is directly involved in Li^+ solvation and has a larger chemical shift range than carbon, the effects reported here are consequently much larger than ^{13}C results [32].

Fundamental considerations of the degree of solvation preference of EC over DMC dictate not only electrolyte bulk properties (e.g. ionic conductivity), but also the mechanism by which the Li^+ ions transition into the SEI and eventually into and out of the intercalation electrodes [30, 34, 35]. EC molecule is distinctly more polar than the linear carbonates (DMC), which becomes favored chemical source for the interfacial ingredients (cyclic and linear carbonates). There is a preference of Li+ ion in binding the more polar molecules from the electrolyte solvent mixture [36].

Chapter 8

Bismuth Fluoride Nanocomposite as a Positive Electrode Material for Rechargeable Lithium Batteries

8.1 Introduction

All of the present state of the art Li-ion batteries operate with positive electrodes based on intercalation reactions. With more than 25 years of research dedicated to them, these reactions are well understood and show excellent performance. Nonetheless, their practical depth of discharge must be limited to relatively low values to remain in the range of reversibility of the active material. In the age of portable technologies, the need for small electrical energy supply devices grows steadily. New materials able to store more energy must be brought to market.

Intercalation compounds do not have large capacity because the intercalation process is not an ideal energy storage mechanism. This situation occurs because of the limited number of vacancies available for lithium resulting in a limited utilization of the oxidation states of the host metal. An alternative process, *reversible conversion*, allows for all the oxidation states of a compound to be utilized [1]. Reversible conversion materials show a constant change in the crystal structures, and a number of nanophases may be present in the lithiated vs. delithiated states. Both of these aspects are especially important when it comes to the impact of electrolyte decomposition products formed on the surface of materials because the ‘‘substrate’’ for these reactions is in a continually dynamic state. To date there has been only limited discussion of solid electrolyte interphase (SEI) formation relative to high voltage conversion materials [2].

For practical cathode applications, the active material must have a conversion reaction output voltage greater than 2 V. For true conversion reaction, this can only be achieved with very ionic compounds [3].

One published article, authored by Fiordiponti et al. (1978) [4], reported an investigation on BiF_3 as positive electrode active material in primary lithium battery applications [5]. BiF_3 CMFNC (Carbon Metal Fluoride Nanocomposites) exhibits some interesting properties for applications as a positive electrode active material in rechargeable lithium batteries [6].

Several reasons lead us to study the BiF_3 CMFNC as a candidate for cathode applications, for instance, its high theoretical output voltage based on the conversion to Bi^0 + 3LiF, at about 3 V [3]. BiF_3 is very dense and has a very attractive volumetric energy density of 7170 Wh/l^{-1}, close to three times higher than $LiCoO_2$ (today’s state of the art cathode material). BiF_3 is also known as a relatively good fluorine ions conductor [7], and that may play an important role in the kinetics of conversion reactions.

A high voltage reversible conversion reaction of BiF_3 was enabled by the creation of a conductive bismuth fluoride nanocomposite utilizing carbon [3]. The creation of the BiF_3/C nanocomposite enables the electrochemical activity of the bismuth trifluoride. The macroscopic BiF_3/C composite exhibited small initial discharge capacity of 40 mAh/

(g of composite) with poor subsequent reversibility. In contrast, the nanocomposite revealed a fully reversible capacity of about 230 mAh/(g of composite).

Bismuth metal fluorides, such as BiF_3, are capable of reversible conversion reaction during lithiation in the BiF_3/C nanocomposite according to the following equation:

$$BiF_3 + 3Li \underset{\text{charge}}{\overset{\text{discharge}}{\rightleftarrows}} Bi^0 + 3LiF \tag{8.1.1}$$

The term *reversible conversion reaction* refers to reactions in which the nanocrystalline bismuth fluoride component of the nanocomposite is capable of reforming during a battery cell charge.

Two lithiation transport mechanism schematics are shown in the Fig. 8.1.1 according to Bervas et. al. (2006) [6]. At the beginning of the lithiation the nanocomposite is composed of BiF_3 nanoparticles surrounded by a carbon matrix. Due to the extremely high porosity of the carbon matrix, one can imagine that the metal fluoride particles are also in direct contact with the electrolyte, enabling facile ionic transport. At that early stage of the reaction, the electrons are transferred to the BiF_3 surface via the carbon matrix and the Li^+ ions migrate to the BiF_3 surface directly from the electrolyte, inducing the surface conversion (reduction) into Bi^0 and LiF (transport mechanism A in Fig. 8.1.1). After a certain degree of completion of the conversion reaction, the entire surface of the BiF_3 particles has been reduced. This point is dependent on the specific surface area of the bismuth fluoride. The nanocomposite is then composed of BiF_3 crystallites of only a few nanometers (<10 nm) surrounded by the conversion reaction products, Bi^0 and LiF, and not by the carbon matrix anymore. At this point the transport mechanisms change dramatically as the Li^+ ion diffusion takes place through the defect boundaries of the LiF and Bi nanocrystallites. Electrons are transferred to the core BiF_3 via percolation (transport mechanism B in Fig. 8.1.1).

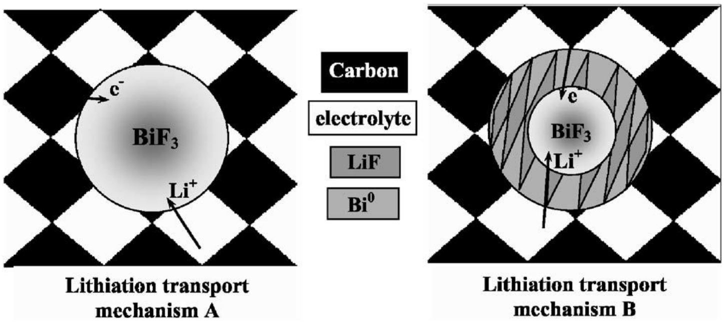

Figure 8.1.1: Schematics of the two different transport mechanisms for the lithiation. Mechanism A (x in "LixBiF3 " < 1.5) and Mechanism B (x in "Li_xBiF_3 " > 1.5) [6].

Such dramatic difference in transport mechanisms could indeed justify a dramatic polarization change, leading to the occurrence of these two pseudo plateaus during the lithiation. Polarization increases with x, going from about 0.1 V at the beginning of the lithiation when the nanocomposite is constituted of BiF_3 nanoparticles surrounded by the carbon matrix, to about 0.3 V at the end of the lithiation when the nanocomposite is constituted of extremely nano BiF_3 particles surrounded by Bi^0 and LiF particles. The polarization is therefore greater with transport mechanism B than with transport mechanism A.

Only the tysonite BiF_3 forms during the delithiation, even when the starting material is the pure orthorhombic BiF_3/C nanocomposite [6]. When the oxidation reaction commences, the Li^+ ions diffuse (migrate) from the LiF nanoparticles near the surface of the aggregates (Bi^0 + LiF) directly into the electrolyte and the electrons are transferred from the Bi^0 nanoparticles near the surface of the (Bi^0 + LiF) aggregates directly to the carbon matrix, inducing the oxidation of the bismuth metal into BiF_3 (transport mechanism A in Fig. 8.1.2). The surface has been fully oxidized and all the (Bi^0 + LiF) aggregates are covered with an electron insulative BiF_3 layer. For the delithiation reaction to proceed the electrons have to tunnel from the remaining Bi^0 nanoparticles to the carbon matrix through the BiF_3 layer and, the Li^+ ions have to diffuse from the remaining LiF nanoparticles to the electrolyte through the BiF_3 layer (transport mechanism B in Fig. 8.1.2).

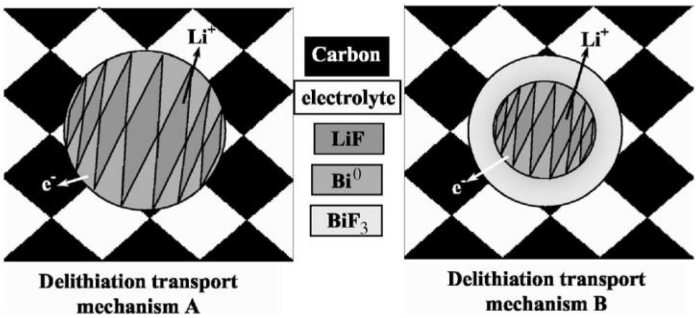

Figure 8.1.2: Schematics of the two different transport mechanisms for the delithiation. Mechanism A (x in "Li_xBiF_3 " > 1) and Mechanism B (x in "Li_xBiF_3 " < 1) [6].

Bismuth compounds that combine both oxides and fluorides, theoretically, can be an attractive alternative to metal fluorides since they combine the high voltage of the fluorides with the higher electronic conductivity of the oxides. Although they exhibit poor cycling stability, the reversible conversion reactions are possible in metal oxyfluoride nanocomposites. However, to date, bismuth oxyfluoride has not been utilized as a positive electrode material in Li-ion battery cells [1].

8.2 Experimental

For this project we are interested in the study of Bismuth Fluoride as cathode material for rechargeable batteries. The objective was to study ^{19}F and ^{7}Li MAS NMR of some nanocomposite cathode materials from the laboratory of Dr. Glenn Amatucci, Rutgers University. According to a previous investigation [1] the cathodes were discharged and charged in Swagelok-style cells with 1M $LiPF_6$ EC:DMC 1:1, a standard electrolyte from Ferro/Novolyte. After galvanostatic trials, the cells were dissembled and the cathodes were soaked for roughly 1h in DMC to remove as much of the $LiPF_6$ as possible. The materials were labeled as:

* Initial nanocomposite (Plain Cathode with no treatment)

* 9_4E 50% discharge

* 9_4F Full discharge (there was a trace of BiF_3 in XRD)

* 9_4G discharge 50% recharge

* 9_4H discharge 60% recharge

* 9_10A Initial nanocomposite 3d soak in 1M $LiPF_6$ EC:DMC 1:1, rinse 3x with DMC

Samples of each material were packed in 1.6 mm rotors inside the glove box, and spun at 37 kHz in the 300MHz Varian Direct Digital Drive Spectrometer. For ^{19}F MAS NMR 3μs was used as 90° pulse width under spin echo sequence with very large d1 (~300 sec) to ensure no saturation. Since the signal was very strong each sample was run only 16 scans. For ^{7}Li MAS NMR 5.5μs was used as 90° pulse under spin echo sequence with large d1 (~100 sec) and each sample was run only 4 scans.

8.3 Results and Discussion

8.3.1 ^{19}F MAS NMR

^{19}F MAS NMR spectra of all the samples except for the starting cathode material are depicted in Fig.8.3.1 at 37 kHz spinning speed. The main peak corresponds to LiF (-202 ppm). The maximum intensity was found for Full discharge (fully lithiated) following for 50% discharge. The intensities of discharge and recharge at 60% and 50% present less LiF as it is expected due to the lithiation and delithiation process. The sidebands of LiF are found at -333 ppm and -70 ppm, respectively. The latter one overlapped with another peak that is assigned to residual arsenic hexafluoride (AsF_6)

from the salt in the electrolyte. This extra peak only appears clearly for Full Discharge sample.

The discharged and recharged materials also show a defined peak at -144 ppm. This peak does not appear for the discharged samples that were not recharged. This peak is presently unassigned. There are another two peaks at -122 ppm (Teflon) and -105 ppm which they can be seen as background intensity from the rotor and Teflon. A second unassigned peak at -26 ppm it found again in recharged materials.

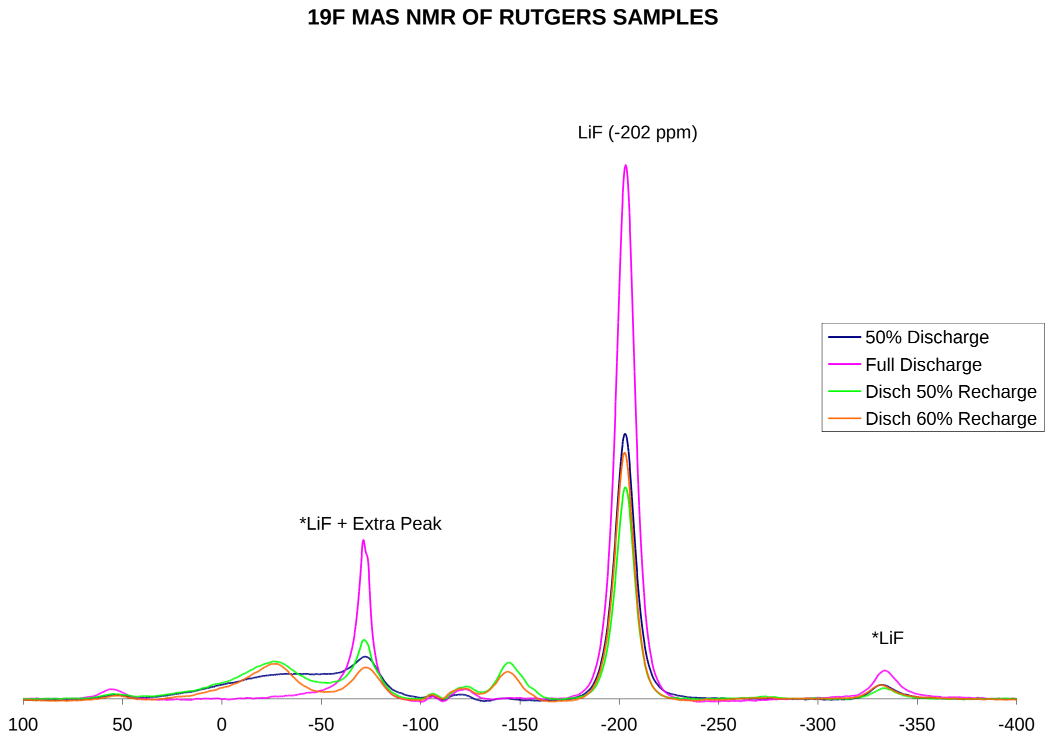

Figure 8.3.1: ^{19}F MAS NMR spectra of all the samples except for the starting cathode material.

^{19}F MAS NMR spectra of only Full discharged and, Discharged and 60% recharged samples were plotted in Fig.8.3.2 at different spinning speed.

Both samples were run at different spinning speed to show the sidebands of LiF and the overlapping peak at -70 ppm.

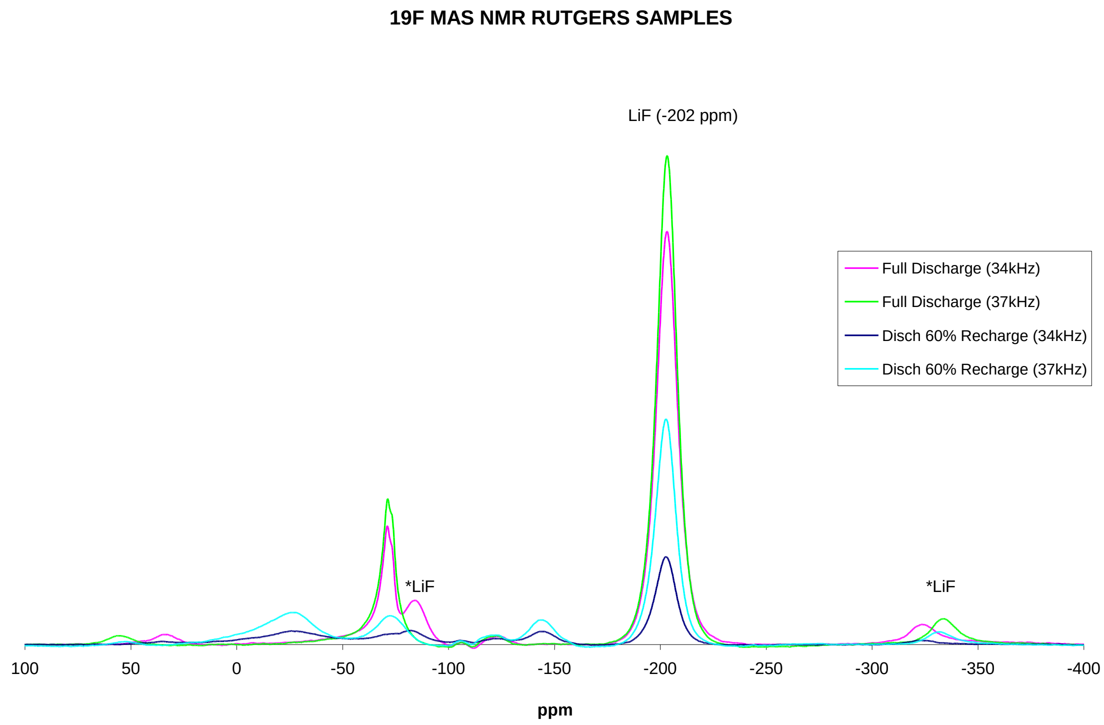

Figure 8.3.2: ^{19}F MAS NMR spectra of only Full discharged and, Discharged and 60% recharged samples.

^{19}F MAS NMR spectra of only starting cathode materials, Plain Cathode and Plain Cathode Rinse three times with DMC to remove as much of the $LiPF_6$ as possible are depicted in Fig.8.3.3.

Both Plain Cathodes showed a trace of Teflon (-123 ppm), and only Plain Cathode Rinse shows a new peak at -154 ppm. This new peak may be some residue of the soak and rinse processes. The main peak is found at -62 ppm for both Plain Cathodes assigned to BiF_3. The big linewidth observed is due to the dipole-dipole interaction between the ^{19}F spins.

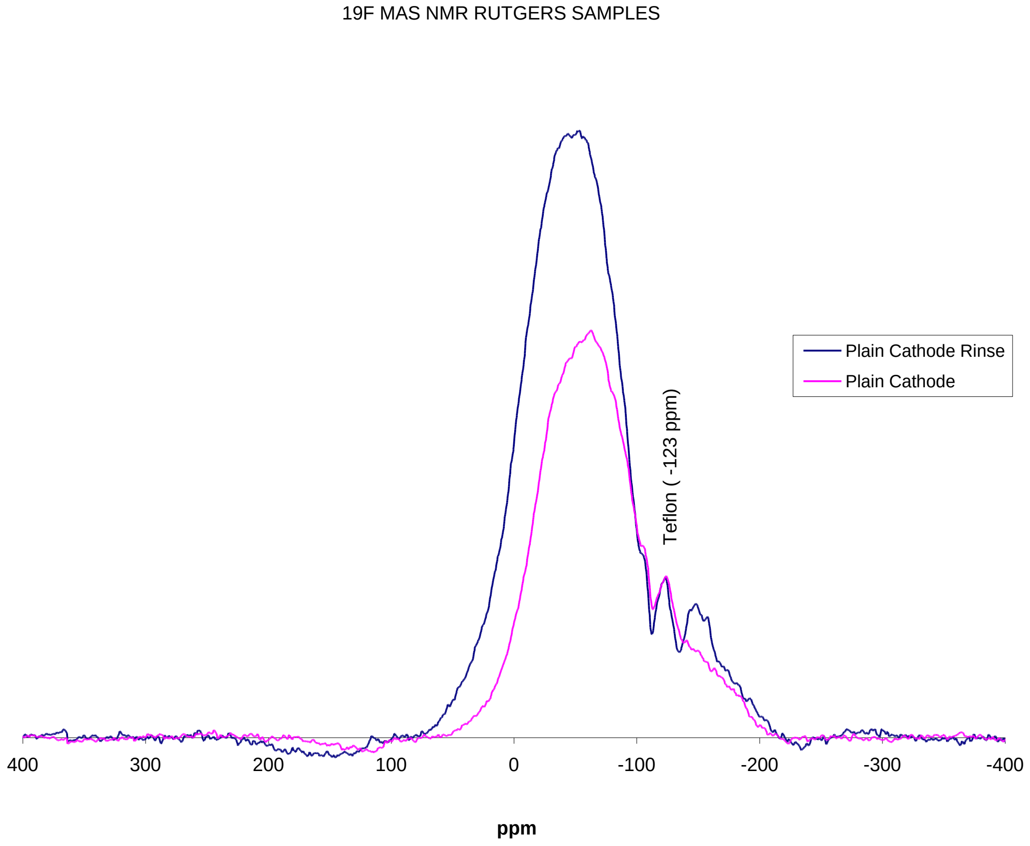

Figure 8.3.3: ^{19}F MAS NMR spectra of only starting cathode materials, Plain Cathode and Plain Cathode Rinse.

^{19}F MAS NMR spectra of all of the samples were plotted in Fig.8.3.4 for comparison.

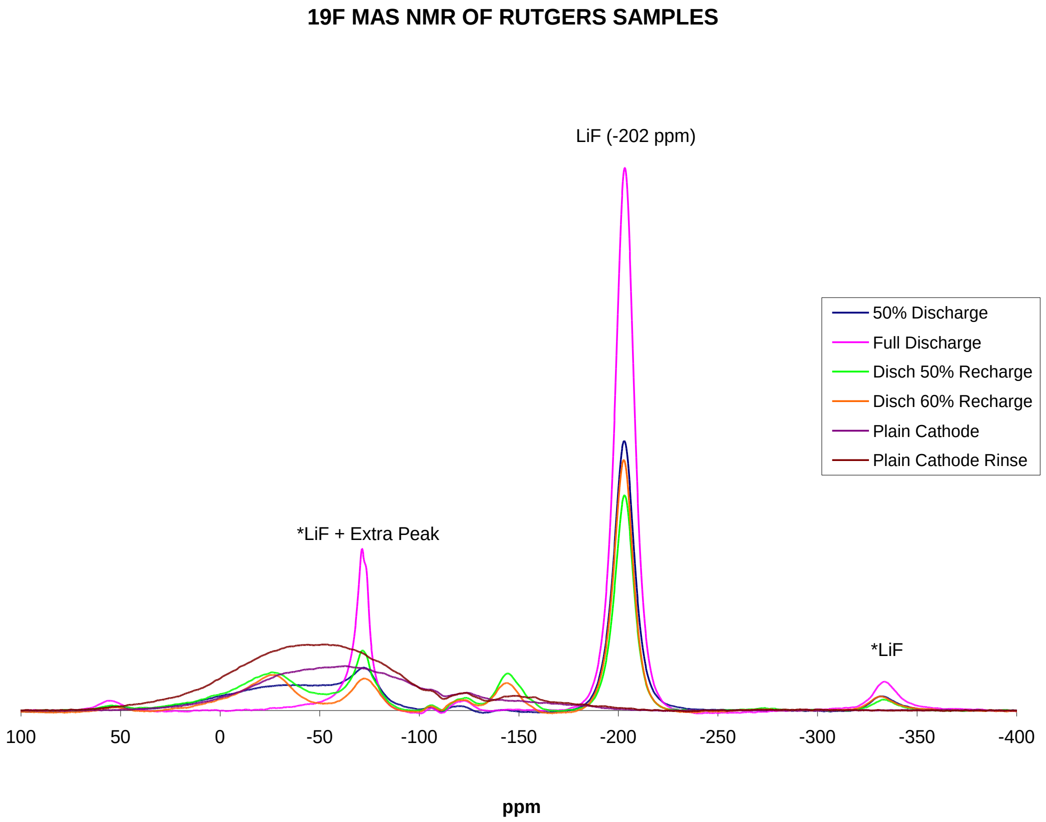

Figure 8.3.4: ^{19}F MAS NMR spectra of all of the samples.

8.3.2 ^{7}Li MAS NMR

^{7}Li MAS NMR spectra of all the samples but starting cathode materials were plotted at 37 kHz and 35 kHz spinning speed are depicted in Fig.8.3.5.

The main peak corresponds to LiF (-1 ppm). The maximum intensity was found for Full Discharge in the process of lithiation.

The sidebands of LiF are found at -318 ppm and +317 ppm. Samples were run at different spinning speed (37 Hz and 35 Hz respectively), so the positions of some sidebands do not align, but still clearly distinguishable.

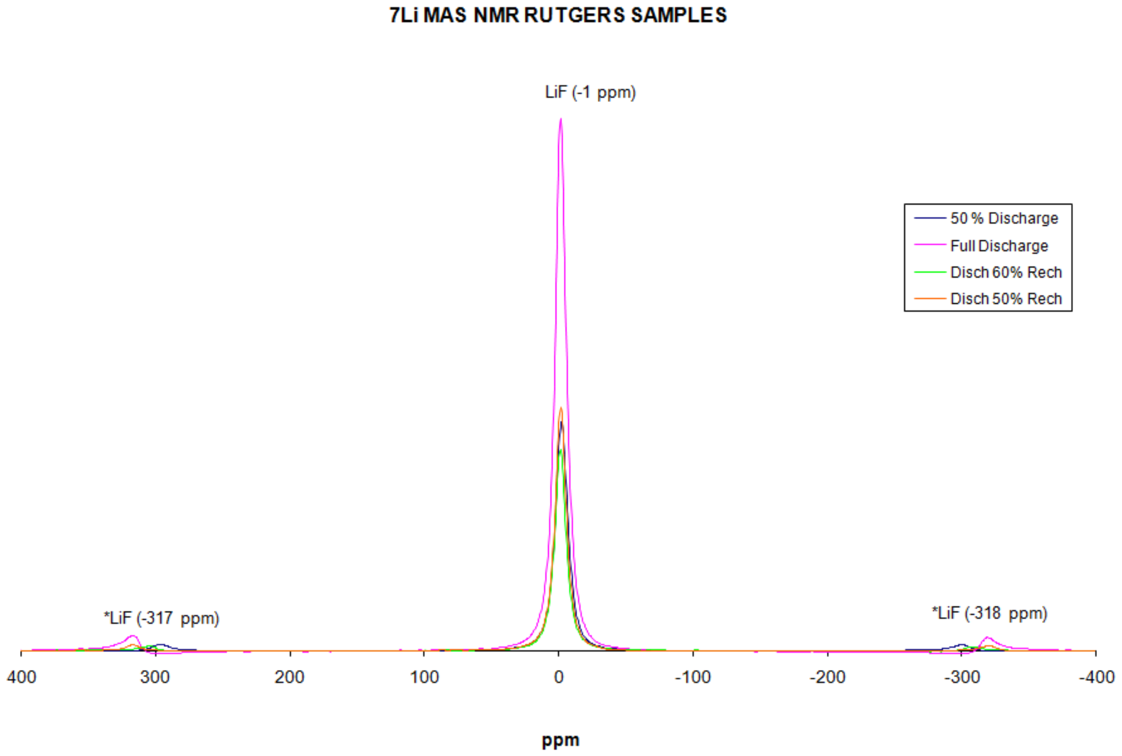

Figure 8.3.5: ^{7}Li MAS NMR spectra of all the samples but starting cathode materials.

8.4 Conclusion

It has been demonstrated that the electrochemical activity of high voltage/high energy density metal fluorides can truly be enabled when prepared in their nanostructured state, and dispersed in a conductive matrix such as carbon or metal oxide. The NMR data confirm that a conversion reaction occurring during lithiation in the BiF_3/C nanocomposite is reversible [5].

The key to the reversibility of the conversion reaction seems to lie in the formation, upon complete reduction of the metal, of nanoparticles that, owing to the large amount of interfacial surface, are very active toward the decomposition of the matrix of the lithium binary compound (Li_nX) in which they are embedded when a reverse polarization is applied. The nanometric character of the metal particles has shown to be maintained even after several reduction-oxidation cycles [8].

Chapter 9

Bibliography

Chapter 1

[1] MacDougall F, Ennis J, Cooper R, Bates J and Seal K. High energy density pulsed power capacitors. IEEE, 1 (2003), 513-7.

Chapter 2

[1] M.-J. Pan, C.A. Randall, IEEE Electrical Insulation Magazine, 26 (2010) 44-50.

[2] Rafael Vazquez-Reina, Sheng Chao, Vladimir Petrovsky, Fatih Dogan, Steven Greenbaum "Electrical and electron paramagnetic resonance spectroscopy characterization of Mn-doped nanostructured TiO_2 for capacitor applications" Journal of Power Sources 210 (2012) 21– 25.

Chapter 3

[1] John A. Weil, James R. Bolton, John E. Werts "Electron Paramagnetic Resonance: Elementary Theory and Practical Applications" Wiley-Interscience Publication, John Wiley & Sons, Inc. ISBN 0471572349.

Chapter 4

[1] Y. Ye, S. Z. Zhang, F. Dogan, E. Schamiloglu, J. Gaudet, P. Castro, M. Roybal, M. Joler, and C. Christodulou, 14th IEEE International Pulsed Power Conference, Dallas, TX, (2003) 719-722.

[2] S. Chao, V. Petrovsky, F. Dogan, J. Am. Ceram. Soc. 93 (2010) 3031-3034.

[3] S. Chao, V. Petrovsky, F. Dogan, J. Mater. Sci. 45 (2010) 6685–6693.

[4] J. Haines and J. N. Léger, Physica B 192 (1993), 233.

[5] Wunderlich, W., Oekermann, T., Miao, L., Hue, N. T., Tanemura, S. and Tanemura, M., J. Ceram. Process. Res., 2004, 4, 342.

[6] Greenwood, Norman N.; Earnshaw, A. (1984), Chemistry of the Elements, Oxford: Pergamon, pp. 1117–19, ISBN 0-08-022057-6

[7] P. Kofstad: "Nonstoichiometry, diffussion, and electrical conductivity in binary metal oxides", Wiley Interscience, New York (1972).

[8] William S. Epling, Charles H.F. Peden, Michael A. Henderson and Ulrike Diebold "Evidence for oxygen adatoms on TiO_2(110) resulting from O_2 dissociation at vacancy sites". Surface Science 412/413 (1998) 333–343.

[9] Tracy L. Thompson and John T. Yates, Jr. "TiO_2-based photocatalysis: surface defects, oxygen and charge transfer". Topics in Catalysis Vol. 35, Nos. 3–4, July 2005 (2005).

[10] F.D. Brandão, M.V.B. Pinheiro, G.M. Ribeiro, G. Medeiros-Ribeiro, and K. Krambrock "Identification of two light-induced charges states of the oxygen vacancy in single-crystalline rutile TiO_2". Physical Review B 80, 235204 (2009).

[11] Myong-Ho Kim, seung-Bong Baek an Ungyu Paik "Electrical Conductivity and Oxygen Diffusion in Nonstoichiometric TiO_{2-x}. Journal of the Korean Physical Society, Vol. 32, February 1998, pp. S1127-S1130.

[12] C. Adan, A. Bahamonde, M. Fernandez-Garcia, A. Martinez-Arias “Structure and activity of nanosized iron-doped anatase TiO_2 catalysts for phenol photocatalytic degradation”. Applied Catalysis B: Environmental 72 (2007) 11–17.

[13] M. Aono and R. R. Hasiguti “Interaction and Ordering of Lattice Defects in Oxygen-deficient rutile TiO_{2-x}“. Physical Review B, Vol. 48, 17 (1993).

[14] A. Templeton, X. Wang, S. J. Penn, S. J. Webb, L. F. Cohen, and N. M. Alford, “Microwave Dielectric Loss of Titanium Oxide” J. Am. Ceram. Soc. 83 [1] 95-100 (2000).

[15] Per-Olof Anderson and Erik L. Kollberg “Extra EPR Spectra of Iron-Doped Rutile”. Physical Review B, Vol. 8, 11 (1973).

[16] Tianzhong Tong, Jinlong Zhang, Baozhu Tian, Feng Chen and, Dannong He “Preparation of Fe^{+3}-doped TiO_2 catalysts by controlled hydrolysis of titanium alkoxide and study on their photocatalytic activity for methyl orange degradation”. Journal of Hazardous Materials 155 (2008) 572–579.

[17] S. Güler, B. Rameev, R.I. Khaibullin, O.N. Lopatin and B. Aktaş ”EPR Study of Mn-implanted single crystal TiO_2”. Journal of Physics: Conference Series 153 (2009) 012052.

[18] Eric N. Coker, Robert W. Thompson, Anthony G. Dixon, and Albert Sacco, Jr.” Preparation of Zeolite X with Low Levels of Iron Impurity from Reaction Mixtures Containing Triethanolamine”. J. Phys. Chem. 1993, 97, 6465-6469.

[19] Cristina Di Valentin, Gianfranco Pacchioni, Annabella Selloni, Stefano Livraghi, and Elio Giamello “Characterization of Paramagnetic Species in N-doped TiO2

Powders by EPR Spectroscopy and DFT Calculations". J. Phys. Chem. B, Vol. 109, No. 23, 2005.

[20] Scot T. Martin, Colin L. Morrison, and Michael R. Hoffmann "Photochemical Mechanism of Size-Quantized Vanadium-Doped TiO_2 Particles". J. Phys. Chem. 1994, 98, 13695-13704.

[21] Nikolaos Guskos, Grzegorz Zolnierkiewicz, Janusz Typek and Monika Bosacka "EPR Study of the $Me_2InV_3O_{11-\delta}$ (Me = Mg, Zn) Compounds". Rev. Adv. Mater. Sci. 14(2007) 125-129.

[22] Terence J. Kemp, Robin A. McIntyre "Transition metal-doped Titanium (IV) dioxide: Characterization and influence on photodegradation of poly(vinyl chloride)". Polymer Degradation and Stability 91 (2006) 165-194.

[23] S. Chao and F. Dogan, "Effect of Manganese Doping on the Dielectric Properties of Titanium Oxide Ceramics" J. Amer. Ceram. Soc. 94 [1] 179-186 (2011).

[24] I. Burn, J. Mater. Sci. 14 (1979) 2453.

Chapter 5

[1] Thomas B. Reddy and David Linden "Handbook of Batteries", McGraw-Hill Third Edition.

[2] D. Guerard, A. Herold, Carbon 1975, 13. 337.

[3] M. S. Whittingham, Prog. Solid State Chem. 1978, 12, 41.

[4] Jordi Cabana, Laure Monconduit, Dominique Larcher, and M. Rosa Palacin, "Beyond Intercalation-Based Li-ion Batteries: The State of the Art and Challenges Materials Reacting Through Conversion Reactions" DOI: 10.1002/adma.201000717.

[5] Thackeray M.M, Thomas J.O, and Whittingham M.S. Science and Applications of Mixed Conductors for Lithium Batteries. Materials Research Society, March 2000.

[6] M. Winter, J.O. Besenhard, M.E. Spahr and P. Novák, Advanced Materials, 10 (1998) 725.

[7] E. Peled, J. Electrochem. Soc., 126 (1979) 2047.

[8] P. Arora, R.E. White and M. Doyle, J. Electrochem. Soc., 145 (1998) 3647.

[9] G. Pistoia, A. Antonini, R. Rosati and D. Zane, Electrochim. Acta, 41 (1996) 2683.

[10] G. Amatucci, C.N. Schmutz, A. Blyr, A. Sigala, A.S. Gozdz, D. Larcher and J.-M. Tarascon, J. Power Sources, 69 (1997) 11.

[11] M. Bervas, F. Badway, L. C. Klein, and G. G. Amatucci, “Bismuth Fluoride Nanocomposite as a Positive Electrode Material for Rechargeable Lithium Batteries” Electrochemical and Solid-State Letters, 8 (4) A179-A183 (2005).

[12] P. Poizot, S. Laruelle, S. Grugeon, L. Dupont, J. M. Tarascon, Nature 2000, 407, 496.

[13] M. Bervas, A. N. Mansour, W.-S. Yoon,d, J. F. Al-Sharab, F. Badway, F. Cosandey, L. C. Klein, and G. G. Amatucci, “Investigation of the Lithiation and Delithiation Conversion Mechanisms of Bismuth Fluoride Nanocomposites” Journal of The Electrochemical Society, 153 (4) A799-A808 (2006).

[14] Andrew J. Gmitter, Fadwa Badway, Sylvie Rangan, Robert A. Bartynski, Anna Halajko, Nathalie Pereira and Glenn G. Amatucci, “Formation, dynamics, and

implication of solid electrolyte interphase in high voltage reversible conversion fluoride nanocomposites" DOI: 10.1039/b923908a.

[15] S. Grugeon, S. Laruelle, L. Dupont, J. M. Tarascon, Solid State Sci. 2003, 5, 895.

[16] M. Bervas, L. C. Klein, and G. G. Amatucci, J. Electrochem. Soc., 153, A159 (2006).

Chapter 6

[1] Levitt, Malcolm H. Spin Dynamics "Spin Dynamics: Basics of Nuclear Magnetic Resonance". John Wiley & Sons, Ltd, 2005.

[2] Joseph P. Hornak, The Basics of NMR, http://www.cis.rit.edu/htbooks/nmr (1997-2008).

[3] Callaghan, P.T. "Principles of NMR Microscopy." Clarendon, Press, Oxford (1991).

[4] Melinda J. Duer, "Solid-State NMR Spectroscopy: Principles and Applications." Blackwell Ltd 2002.

Chapter 7

[1] S. Yoda and K. Ishihara, J. Power Sources, 68 (1997) 3.

[2] J.O. Besenhard, M. Winter, J. Yang and W. Biberacher, J. Power Sources, 54 (1995) 228.

[3] E. Peled, J. Electrochem. Soc., 126 (1979) 2047.

[4] D. Aurbach, B. Markovsky, A. Schechter and Y. Ein-Eli, J. Electrochem. Soc., 143 (1996) 3809.

[5] G. Hong and E.S. Takeuchi, J. Power Sources, 62 (1996) 45.

[6] Linden, D., Ed. Handbook of Batteries, 3rd ed, McGraw-Hill, New York, 2001.

[7] Kang Xu "Nonaqueous Liquid Electrolytes for Lithium-Based Rechargeable Batteries" Chem. Rev. 2004, 104, 4303-4417.

[8] J. Barthel, H.-J. Gores, in: G. Mamantov, A.I. Popov (Eds.), Chemistry of Nonaqueous Solutions Current Progress, VCH publiaher Inc, 1994, p. 1.

[9] H. Ohtaki, S. Ishiguro, in: G. Mamantov, A.I. Popov (Eds.), Chemistry of Nonaqueous Solutions Current Progress, VCH publiaher Inc, 1994, p. 179.

[10] Ding, M. S.; Xu, K.; Zhang, S.; Jow, T. R. J. Electrochem. Soc. 2001, 148, A299.

[11] Tobishima, S.; Arakawa, M.; Hirai, T.; Yamaki, J. J. Power Sources 1989, 26, 449.

[12] McMillan, R. S.; Juskow, M. W. J. Electrochem. Soc. 1991, 138, 1556.

[13] D. Aurbach, Nonaqueous Electrochemistry, Marcel Dekker, Inc., New York (1999).

[14] K. Kanamura, S. Shiraishi and Z.-i. Takehara, J. Electrochem. Soc., 143 (1996) 2187.

[15] K. Kanamura, H. Tamura, S. Shiraishi and Z.-i. Takehara, J. Electrochem. Soc., 141 (1994) 2379.

[16] L.J. Krause, W. Lamanna, J. Summerfield, M. Engle, G. Korba and R. Loch, J. Power Sources, 68 (1997) 320.

[17] K. Nagayama, K. Kamioka, E. Iwata, H. Oka, Y. Tokunaga and T. Okada, Electrochemistry, 69 (2001) 6.

[18] A.A. Smagin, V.A. Matyuka and V.P. Korobtsev, J. Power Sources, 68 (1997) 326.

[19] X. Zhang, P.N. Ross, R. Kostecki, F. Kong, S. Sloop, J.B. Kerr, K. Streibel, E.J. Cairns and F. McLarnon, J. Electrochem. Soc., 148 (2001) A463.

[20] A. DuPasquier, A. Blyr, P. Courjal, D. Larcher, G. Amatucci, B. Gérand and J.-M. Tarascon, J. Electrochem. Soc., 146 (1999) 428.

[21] Ue, M.; Takeda, M.; Takehara, M.; Mori, S. J. Electrochem. Soc. 1997, 144, 2684.

[22] Tarascon, J. M.; Guyomard, D. Solid State Ionics 1994, 69, 293.

[23] Levitt, Malcolm H. Spin Dynamics “Spin Dynamics: Basics of Nuclear Magnetic Resonance”. John Wiley & Sons, Ltd, 2005.

[24] I.P. Gerothanassis, Progr. NMR Spectrosc. 19 (1987) 267.

[25] M.L. Buess, G.L. Petersen, Rev. Sci. Instrum. 49 (1978) 1151.

[26] P.S. Belton, I.J. Cox, R.K. Harris, J. Chem. Soc., Faraday Trans. 2 (81) (1985) 63.

[27] I.P. Gerothanassis, J. Lauterwein, J. Magn. Reson. 66 (1986) 32.

[28] Dahn, H.; J. Chem. Educ., 2000, 77 (7), 905.

[29] Raos, G.; Castiglione, F.; Baggioli, A.; Citterio, A.; Mele, A.; J. Phys. Chem. A. 2012, 116, 1814.

[30] Xu, K.; von Cresce, A., Electrochem. Solid-State Lett., 2011, 14(10), A154.

[31] Marchington, A.F.; Moore, S.C.R.; Richards, W.G.; J. Am. Chem. Soc. 1979, 101, 5529.

[32] Li Yang, Ang Xiao, Brett L. Lucht “Investigation of salvation in lithium ion battery electrolytes by NMR spectroscopy” Journal of Molecular Liquids 154 (2010) 131-133.

[33] (a)Cavaleiro, J. A. S.; J. Chem. Educ. 1987, 64 (6), 549. (b) Gunther, H.; NMR Spectroscopy.; Wiley: New York, 1980; p89. (c) Buckingham, A.D.; Schaeffer, T.; Schneider, W.G.; J. Chem. Phys. 1960, 32(4), 1227.

[34] Xu, K.; von Cresce, A.; Lee, U, Langmuir, 2010, 26, 11538.

[35] Yamada, Y.; Sagane, F.; Iriyama, Y.; Abe, T.; Ogumi, Z. J. Phys. Chem. C 2009, 113, 14528.

[36] Kang Xu, Yiufai Lam, Sheng S. Zhang, T. Richard Jow, and Timothy B. Curtis "Solvation Sheath of Li+ in Nonaqueous Electrolytes and Its Implication of Graphite/Electrolyte Interface Chemistry" J. Phys. Chem. C 2007, 111, 7411-7421.

Chapter 8

[1] Glenn G. Amatucci, and Mathieu Bervas, "Bismuth Oxyfluoride Based Nanocomposites as Electrode Materials" US 2007/0190414 A1 (2007).

[2] Andrew J. Gmitter, Fadwa Badway, Sylvie Rangan, Robert A. Bartynski, Anna Halajko, Nathalie Pereira and Glenn G. Amatucci, "Formation, dynamics, and implication of solid electrolyte interphase in high voltage reversible conversion fluoride nanocomposites" DOI: 10.1039/b923908a.

[3] M. Bervas, F. Badway, L. C. Klein, and G. G. Amatucci, "Bismuth Fluoride Nanocomposite as a Positive Electrode Material for Rechargeable Lithium Batteries" Electrochemical and Solid-State Letters, 8 (4) A179-A183 (2005).

[4] P. Fiordiponti, S. Panero, G. Pistoia, and C. Temperoni, J. Electrochem. Soc.,125, 511 (1978).

[5] M. Bervas, L. C. Klein, and G. G. Amatucci, “Reversible Conversion Reactions with Lithium in Bismuth Oxyfluoride Nanocomposites” J. Electrochem. Soc., 153, A159 (2006).

[6] M. Bervas, A. N. Mansour, W.-S. Yoon,d, J. F. Al-Sharab, F. Badway, F. Cosandey, L. C. Klein, and G. G. Amatucci, “Investigation of the Lithiation and Delithiation Conversion Mechanisms of Bismuth Fluoride Nanocomposites” Journal of The Electrochemical Society, 153 (4) A799-A808 (2006).

[7] C. Julien, G. A. Nazri in Solid State Batteries: Materials Design and Optimization, Kluver Academic, New York.

[8] Jordi Cabana, Laure Monconduit, Dominique Larcher, and M. Rosa Palacin “Beyond Intercalation-Based Li-ion Batteries: The State of the Art and Challenges of Electrode Materials Reacting Through Conversion Reactions” Adv. Mater. 2010, XX, E1-E23, DOI: 10.1002/adma.201000717.